

# UC Berkeley

## UC Berkeley Previously Published Works

### Title

Forced and unforced decadal behavior of the interhemispheric SST contrast during the instrumental period (1881–2012): contextualizing the abrupt shift around 1970 Forced and unforced decadal behavior of the interhemispheric SST contrast during the in...

### Permalink

<https://escholarship.org/uc/item/9k33d7dg>

### Journal

Journal of Climate, 33(9)

### ISSN

0894-8755

### Authors

Friedman, Andrew R  
Hegerl, Gabriele C  
Schurer, Andrew P  
[et al.](#)

### Publication Date

2020

### DOI

10.1175/jcli-d-19-0102.1

Peer reviewed



1 **Forced and unforced decadal behavior of the interhemispheric SST contrast during the**  
2 **instrumental period (1881–2012): contextualizing the abrupt shift around 1970**

3 Andrew R. Friedman<sup>1</sup>, Gabriele C. Hegerl<sup>1</sup>, Andrew Schurer<sup>1</sup>, Shih-Yu Lee<sup>2</sup>, Wenwen Kong<sup>3</sup>,  
4 Wei Cheng<sup>4</sup>, and John C. H. Chiang<sup>3</sup>

5 Resubmission to *Journal of Climate*, 6 December 2019

6

7 <sup>1</sup>School of Geosciences, University of Edinburgh, Edinburgh, United Kingdom

8 <sup>2</sup>Research Center for Environmental Changes, Academia Sinica, Taipei, Taiwan

9 <sup>3</sup>Department of Geography, University of California, Berkeley, California, USA

10 <sup>4</sup>Joint Institute for the Study of the Atmosphere and Ocean, University of Washington, USA

11

12 Corresponding author: Andrew R. Friedman. Crew Building, The King's Buildings, Alexander

13 Crum Brown Road, Edinburgh EH9 3FF, United Kingdom. <[andrew.friedman@ed.ac.uk](mailto:andrew.friedman@ed.ac.uk)>

14 ORCID ID <https://orcid.org/0000-0001-6994-2037>

15

16 **Abstract**

17 The sea surface temperature (SST) contrast between the northern hemisphere (NH) and southern  
18 hemisphere (SH) influences the location of the intertropical convergence zone (ITCZ) and the  
19 intensity of the monsoon systems. This study examines the contributions of external forcing and  
20 unforced internal variability to the interhemispheric SST contrast in HadSST3 and ERSSTv5  
21 observations, and 10 models from the Coupled Model Intercomparison Project Phase 5 (CMIP5)  
22 from 1881–2012. Using multimodel mean fingerprints, a significant influence of anthropogenic,  
23 but not natural, forcing is detected in the interhemispheric SST contrast, with the observed  
24 response larger than that of the model mean in ERSSTv5. The forced response consists of  
25 asymmetric NH–SH SST cooling from the mid 20<sup>th</sup> century to around 1980, followed by  
26 opposite NH–SH SST warming. The remaining best-estimate residual or unforced component is  
27 marked by NH–SH SST maxima in the 1930s and mid 1960s, and a rapid NH–SH SST decrease  
28 around 1970. Examination of decadal shifts in the observed interhemispheric SST contrast  
29 highlights the shift around 1970 as the most prominent from 1881–2012. Both NH and SH SST  
30 variability contributed to the shift, which appears not to be attributable to external forcings. Most  
31 models examined fail to capture such large-magnitude shifts in their control simulations, though  
32 some models with high interhemispheric SST variability are able to produce them. Large-  
33 magnitude shifts produced by the control simulations feature disparate spatial SST patterns,  
34 some of which are consistent with changes typically associated with the Atlantic Meridional  
35 Overturning Circulation (AMOC).

## 36 **1. Introduction**

37 The north–south interhemispheric surface temperature contrast is an important influence on  
38 the location of the intertropical convergence zone (ITCZ) and the strength of the African and  
39 Asian monsoons (Folland et al. 1986; Mantsis and Clement 2009; Chiang and Friedman 2012;  
40 Hwang et al. 2013; Sun et al. 2013; Schneider et al. 2014); as well as the extratropical circulation  
41 (Xue et al., 2018). Previous studies have identified the role of different forcings that have  
42 contributed to changes in the interhemispheric temperature contrast over the instrumental period  
43 (Drost and Karoly, 2012; Friedman et al., 2013). For combined land and ocean surface  
44 temperatures, stronger northern hemisphere (NH) than southern hemisphere (SH) warming is a  
45 robust transient climate response to greenhouse gas (GHG) forcing, largely due to the greater NH  
46 landmass extent and thus smaller thermal inertia (Stouffer et al. 1989; Xu and Ramanathan  
47 2012). Arctic amplification processes also contribute to greater transient NH warming (Serreze  
48 and Barry, 2011). In contrast, the transient warming in the Southern Ocean is limited by  
49 upwelling, the thermal isolation of Antarctica from the Antarctic Circumpolar Current, and the  
50 Southern Ocean meridional overturning circulation (Hutchinson et al., 2013; Marshall et al.,  
51 2014; Armour et al., 2016). Northward heat transport by the Atlantic Meridional Overturning  
52 Circulation (AMOC) is the main cause of the mean positive NH–SH temperature contrast  
53 (Feulner et al., 2013; Kang et al., 2014), and a decreasing AMOC is projected to weaken the  
54 interhemispheric temperature contrast in moderate-emissions future climate projections (Feulner  
55 et al., 2013).

56 Due to their sources mainly in the NH and their relatively short atmospheric residence times,  
57 anthropogenic aerosol emissions contribute to North Atlantic cooling and a decreased NH–SH  
58 interhemispheric temperature contrast (Kiehl and Briegleb 1993; Rotstayn and Lohmann 2002;

59 Chang et al. 2011; Allen et al. 2015; Chung and Soden 2017). Though the magnitude of mid-20<sup>th</sup>  
60 century aerosol forcing remains uncertain (Stevens, 2015; Kretzschmar et al., 2017; Booth et al.,  
61 2018), historical climate model simulations suggest that the positive NH–SH surface temperature  
62 imbalance from GHG forcing overtook the aerosol-related NH–SH decrease around 1980 (Drost  
63 and Karoly, 2012; Friedman et al., 2013; Wilcox et al., 2013; Undorf et al., 2018), with  
64 uncertainty on exact timing due to internal variability and intermodal differences (Schurer et al.,  
65 2018). This reflects North American and European clean air legislation in the 1970s and  
66 continued GHG emissions. Asian sulfate aerosol emissions have also steadily increased since the  
67 1950s, though present-day global emissions do not exceed 1970s estimates (Lamarque et al.,  
68 2010; Hoesly et al., 2018). Asian and African black carbon aerosol emissions have also increased  
69 during this period; their overall radiative forcing is uncertain but estimated to be positive,  
70 spatially and less hemispherically asymmetric compared to sulfate (Bond et al., 2013; Boucher et  
71 al., 2013; Wang et al., 2016). Future anthropogenic aerosol declines are projected to expose even  
72 larger NH warming in the coming decades (Rotstayn et al. 2013; Rotstayn et al. 2015). Another  
73 interhemispheric forcing is stratospheric ozone depletion, which may have stalled SH high-  
74 latitude warming (Marshall et al., 2014).

75 Despite the above progress in physical understanding of the interhemispheric temperature  
76 contrast, key questions remain about the roles of forced and unforced interhemispheric  
77 temperature variability during the instrumental period. Notably, studies have identified a shift in  
78 the interhemispheric temperature difference from the late 1960s through the early 1970s, which  
79 had wide-ranging hydrological impacts particularly on Asian and West African monsoon rainfall  
80 (Baines and Folland, 2007; Dima and Lohmann, 2010; Thompson et al., 2010; Liu and Chiang,  
81 2012). Thompson et al. (2010) do not find any instrumental SST biases at the time of the shift,

82 and use an analytical adjustment methodology to show the drop was unrelated to El Niño /  
83 Southern Oscillation (ENSO) fluctuations, volcanic eruptions, or advection by wintertime  
84 atmospheric circulation. Due to the rapid timescale of the drop and association with a rapid  
85 freshening known as the Great Salinity Anomaly (Dickson et al., 1988), it has been proposed that  
86 the interhemispheric shift was caused by internal ocean variability, notably a shift in the AMOC  
87 (Dima and Lohmann, 2010; Thompson et al., 2010), possibly as part of a longer-term decline  
88 over the 20<sup>th</sup> century driven by Greenland and Arctic meltwater (Rahmstorf et al., 2015; Caesar  
89 et al., 2018). However, this period also coincides with strong sulfate aerosol forcing (Terray,  
90 2012; Friedman et al., 2013; Wilcox et al., 2013; Hodson et al., 2014; Allen et al., 2015). Since  
91 the magnitude of interhemispheric temperature shifts has not been explicitly quantified, it is  
92 difficult to express how unusual the 1970 shift was compared to earlier periods, or if climate  
93 models are able to produce comparable shifts. At the millennial timescale, there have been  
94 indications that climate models may underestimate interhemispheric temperature variability in  
95 paleoclimate reconstructions, through some of the discrepancies may be due to data uncertainties  
96 (Neukom et al., 2014, 2018).

97 This study aims to characterize the decadal variability of the interhemispheric temperature  
98 contrast (focusing on SST only) in a quantitative framework so that the magnitude of the 1970  
99 shift and other changes can be evaluated more rigorously. We employ a regression-based climate  
100 change detection and attribution approach (Hegerl et al. 1997; Allen and Stott 2003) to extract  
101 the forced and unforced components of the interhemispheric SST contrast. We also examine NH  
102 and SH SST separately to understand their respective contributions to interhemispheric SST  
103 variability. Furthermore, we quantify decadal interhemispheric SST shifts using running linear  
104 trends and examine the spatial patterns associated with the largest-magnitude trends, analogous

105 to the approach used in recent studies to quantify the early-2000s global mean surface  
106 temperature slowdown or *hiatus* (Meehl et al. 2011; Schurer et al. 2015; Marotzke and Forster  
107 2015; Medhaug et al. 2017).

108 The paper is organized as follows: In **Section 2**, we present the datasets and simulations  
109 investigated. **Section 3** describes the characteristics of decadal interhemispheric SST variability.  
110 The detection and attribution analysis is applied to the interhemispheric SST contrast in **Section**  
111 **4**. The separate NH and SH components of interhemispheric SST variability are examined in  
112 **Section 5**. **Section 6** focuses on decadal shifts in the interhemispheric SST contrast. Finally,  
113 **Section 7** concludes with the implications of our work plus some open questions.

114

## 115 **2. Data and models**

116 We define the interhemispheric SST contrast anomaly as the anomaly of mean NH minus  
117 mean SH SST; the annual mean is shown in **Figure 1a** (top). We examine SST monthly fields  
118 from the Met Office Hadley Center SST dataset (HadSST3) (Kennedy et al. 2011a, 2011b) and  
119 the NOAA Extended Reconstructed SST dataset, version 5 (ERSSTv5) (Huang et al., 2017).  
120 HadSST3 and ERSSTv5 are both constructed from *in situ* data using much of the same sources,  
121 but apply different quality control, bias corrections, and homogenization. One difference is that  
122 ERSSTv5 infills missing data using empirical orthogonal teleconnections, whereas the HadSST3  
123 data are not infilled. Annual means are taken from December–November, which better fit  
124 climatological seasons and the ENSO annual cycle, and are calculated from 3-month seasonal  
125 means (constructed if there is at least one month of data): December–February, March–May,  
126 June–August, and September–November.

127 Previous studies on the interhemispheric temperature contrast have often examined the  
128 combined land surface and SST interhemispheric temperature contrast (Drost and Karoly 2012;  
129 Friedman et al. 2013; Feulner et al. 2013; Wilcox et al. 2013). In comparison to the  
130 interhemispheric SST contrast, the interhemispheric contrast in land surface temperature, shown  
131 using the Climate Research Unit database (CRUTEM4) (Morice et al., 2012) and the NASA  
132 GISS Surface Temperature Analysis (GISTEMP) (Hansen et al., 2010) (250 km smoothing  
133 version) (**Figure 1a**, bottom), has larger interannual variability and a stronger long-term trend.  
134 As our focus is decadal variability, we hereafter investigate the interhemispheric SST contrast.  
135 While using SST minimizes the direct response of the land surface, we still expect some  
136 contribution from advection from land, especially over the NH (Thompson et al., 2009).

137 We also examine output from the Coupled Model Intercomparison Project Phase 5 (CMIP5)  
138 (Taylor et al. 2012), listed in **Table 1**. We select all model realizations for which both historical  
139 natural forcing (solar and volcanic, referred to as historicalNat) and the corresponding historical  
140 all-forcing (natural and anthropogenic, including GHGs, aerosols, ozone, and land use; referred  
141 to as historical) experiments are available from 1881–2012 to allow the longest possible period  
142 for the detection and attribution analysis. In total, 36 historical and historicalNat realizations  
143 from 10 different models are investigated. For 6 models, output was available from the historical  
144 or the historical extension (historicalExt) experiments from 2006–2012. For 4 models (IPSL-  
145 CM5A-LR, IPSL-CM5A-MR, CSIRO-Mk3-6-0, and one realization of HadGEM2-ES), the  
146 historical experiments end in 2005, so the Representative Concentration Pathway 4.5 (RCP4.5)  
147 experiment output (Vuuren et al., 2011) is used from 2006–2012.

148 We investigate SST from the corresponding pre-industrial control (piControl) runs of each  
149 CMIP5 model, whose lengths are also indicated in **Table 1**. Control simulations from two



150 additional models, NCAR CCSM4 and GFDL-CM3, are also examined in some analyses.  
151 Though model drift has been found to affect some variables in CMIP5 models (Sen Gupta et al.,  
152 2013), our results for the interhemispheric SST contrast are not affected by linear detrending of  
153 the control runs (not shown).

154 The  $2^\circ \times 2^\circ$  ERSSTv5 data and differing-resolution CMIP5 model output are interpolated onto  
155 the  $5^\circ \times 5^\circ$  HadSST3 grid. In computing hemispheric means, the datasets and models are masked  
156 where HadSST3 contains no data in more than 15 of the first 60 years of the study (1881–1940),  
157 shown in **Figure 1b**. [The land surface temperature data in **Figure 1a** (bottom) are masked using  
158 a similar threshold based on the 1881–1940 CRUTEM4 coverage]. Hemispheric means are  
159 calculated poleward of  $5^\circ$  latitude, as modes of interhemispheric SST variability are generally  
160 not centered directly on the equator (Servain et al., 1999; Xie and Carton, 2004; Baines and  
161 Folland, 2007).

162

### 163 **3. Observed and modeled interhemispheric SST variability**

164 As our focus is on decadal and multidecadal variability, we apply a 3-year running mean to  
165 the annual data to suppress high-frequency variations such as ENSO (Wang et al. 2012; Dai  
166 2013). The 3-year mean 1881-2012 observational interhemispheric SST anomaly time series are  
167 shown in **Figure 1c**, along with those of the CMIP5 historical realizations and their ensemble  
168 mean. The observational datasets are highly correlated ( $r=0.92$ ), and generally remain within the  
169 envelope of the historical simulations. The ensemble mean has a long-term negative trend until  
170 around 1980 followed by a rebound, similar to the combined interhemispheric land and SST  
171 difference due to opposing GHG and anthropogenic aerosol forcings (Friedman et al. 2013;  
172 Wilcox et. al. 2013) albeit with a smaller trend since 1980. The amplitude of the ensemble mean

173 variations is expectedly smaller than that of the observations; the latter show a rapid north–south  
174 increase in the 1920s and north–south decrease from the late-1960s to early 1970s.

175 The 1881–2012 standard deviation of the 3-year mean interhemispheric SST contrast of the  
176 observations and historical simulations is shown in **Figure 1d**. The standard deviation of  
177 ERSSTv5 (0.13°C) is larger than that of HadSST3 (0.12°C); both are larger than the multimodel  
178 mean of standard deviations (0.11°C), though still within the inter-model range. An outlier is  
179 GISS-E2-H, whose standard deviations cluster between 0.07°C and 0.08 °C. The single-  
180 realization models (particularly bcc-csm1-1) also have low standard deviations, though we would  
181 need more realizations to evaluate their spread. Similar results are found with further smoothing,  
182 with a relatively larger spread of model standard deviations (not shown).

183 The spatial patterns corresponding to the interhemispheric SST contrast in observations are  
184 shown in **Figures 2a** and **2c**, obtained by ordinary least squares (OLS) regression of the 3-year  
185 mean gridded observations onto the interhemispheric SST time series from 1881-2012. Slope  
186 significance is evaluated using a 2-tailed *t*-test, adjusting for temporal autocorrelation by  
187 increasing the regression standard error by a factor of  $\sqrt{3}$  assuming 1 degree of freedom for  
188 every 3 years of length (Santer et al., 2000; Biasutti et al., 2008). We additionally apply a False  
189 Discovery Rate (FDR) procedure to test for field significance (Genovese et al., 2002; Wilks,  
190 2016), stippling the gridpoints with *p*-values satisfying the FDR criterion  $\alpha_{\text{FDR}} = 0.05$ . Both  
191 datasets have prominent significant positive slopes over the subpolar North Atlantic and  
192 significant negative slopes in the extratropical South Atlantic and South Indian oceans.  
193 ERSSTv5 has more significant gridboxes, presumably due to its reduced spatial noise. Negative  
194 Indian Ocean slopes extend into the NH, similar to the interhemispheric SST mode in Parker et

195 al. (2007). There are also positive slopes in the mid-latitude North Pacific, albeit not significant  
196 in either dataset.

197 **Figure 2e** shows the 1881-2012 ensemble mean spatial pattern of the 3-year mean CMIP5  
198 historical interhemispheric SST contrast, calculated as the ensemble mean of the regression  
199 slopes of each gridded realization's SST field onto its own interhemispheric SST contrast time  
200 series (the thin lines in **Figure 1c**). The slopes are stippled where at least 30 of the 36  
201 realizations agree on the sign of the slope. In contrast to the observations, the strongest  
202 amplitudes and model agreement are in the mid-latitude North Pacific, with maximum slopes  
203 over the Kuroshio extension. The models show consistent negative slopes in the extratropical  
204 SH, particularly the mid-latitude Atlantic and Indian oceans around 40°–45°S.

205 To illustrate the hydrologic impacts of interhemispheric SST variability, we show the spatial  
206 patterns of tropical rainfall associated with the interhemispheric SST contrast. **Figures 2b** and **2d**  
207 show the regression slopes of 3-year mean rainfall over land using the Global Precipitation  
208 Climatology Center (GPCC) 2.5° spatially-infilled full data monthly product, version 2018  
209 (Becker et al. 2013; Schneider et al. 2018) onto the interhemispheric SST contrast. The observed  
210 slopes are calculated from 1930–2012 due to insufficient gauge coverage beforehand (Polson et  
211 al. 2016). Slopes are stippled where significant at  $p < 0.05$  using a 2-tailed  $t$ -test, adjusted for  
212 temporal autocorrelation and applying the FDR procedure similarly as the SST data in **Figures**  
213 **2a** and **2c**. The right panels show the zonal mean slopes. **Figure 2f** shows the 1930-2012  
214 ensemble mean slope of CMIP5 historical precipitation over land and ocean regressed onto the  
215 interhemispheric SST contrast, with the precipitation fields regridded onto a common 2.5° grid.  
216 Stippling indicates sign agreement of at least 30 of 36 realizations as in **Figure 2e**. The zonal

217 mean slopes in **Figure 2f** are shown both globally and for land regions only (masked to the  
218 GPCC grid), with the distribution of the middle 30 realizations indicated.

219 Both the observations and the models show displacement of tropical rainfall into the warmer  
220 SST hemisphere (Chung and Ramanathan, 2007; Chiang and Friedman, 2012; Sun et al., 2013),  
221 with observational slope significance and high model agreement found in the ITCZ and monsoon  
222 regions, emphasizing the strong imprint of the interhemispheric SST contrast on these rainfall  
223 features. However, almost all the realizations underestimate the zonal mean slope magnitudes in  
224 northern tropical land region around 10°N (largely reflecting Africa), consistent with larger-  
225 magnitude observed 20<sup>th</sup> century changes compared to most CMIP3 and CMIP5 models (Hwang  
226 et al., 2013; Polson et al., 2014; Hegerl et al., 2015).

227

#### 228 **4. Attribution of interhemispheric SST variability to forcing**

229 In this section, we conduct a detection and attribution analysis to identify the forced  
230 components of the 3-year running mean interhemispheric SST contrast shown above.

231

##### 232 *4.1 Detection and attribution methodology*

233 Detection and attribution provides a rigorous framework to separate the components of  
234 observed climate changes driven by external forcing and internal variability (e.g. Hegerl et al.  
235 1997; Allen and Stott 2003). A typical assumption of regression-based detection and attribution  
236 studies such as used here is that the spatiotemporal response pattern of an external forcing is  
237 much better known than the response magnitude (Bindoff et al., 2013). Here, we apply total least  
238 squares (TLS) regression for detection and attribution of the interhemispheric SST contrast  
239 (Allen and Stott 2003). We use multimodel ensemble mean fingerprints, which have often been

240 found to perform better than any individual model (Knutti et al. 2010; Hegerl and Zwiers 2011),  
241 though may underestimate the role of model uncertainty (Schurer et al., 2018). Equal weight is  
242 given to each of the 36 realizations in constructing the multimodel ensemble mean. Calculating  
243 the mean over the available simulations rather than among individual models results in a greater  
244 signal-to-noise ratio, though it means that some models are given greater weight due to having  
245 more realizations.

246 We apply a two-signal analysis with historical and historicalNat fingerprints to detect net  
247 anthropogenic forcing, which has been found to be more robust than detecting aerosol and GHG  
248 forcing separately (Bindoff et al. 2013; Jones et al. 2016). The observations and fingerprints are  
249 shown in **Figure 3a**. As in Schurer et al. (2013), the fingerprints are not optimized. The scaling  
250 coefficients  $\beta_1$  and  $\beta_2$ , which determine the magnitude of the fingerprints from observations, are  
251 calculated as follows:

$$252 \quad y = \beta_1(X_{historicalNat} - \varepsilon_{historicalNat}) + \beta_2(X_{historical} - \varepsilon_{historical}) + \varepsilon_{obs} \quad , \quad (1)$$

253 where  $y$  is the observed interhemispheric SST contrast time series of length  $L$  (132 years  
254 excluding endpoints due to smoothing: 130 years);  $X_{historicalNat}$  and  $X_{historical}$  are the length- $L$   
255 multimodel mean fingerprints;  $\varepsilon_{historicalNat}$  and  $\varepsilon_{historical}$  are the length- $L$  internal variability of  
256 each fingerprint; and  $\varepsilon_{obs}$  is the unforced residual variability. We assume that taking the mean  
257 over  $n$  ensemble members (36 realizations) reduces the internal variability by a factor of  $\sqrt{n}$ .

258 We rearrange  $\beta_1$  and  $\beta_2$  into natural ( $\beta_{Nat}$ ) and anthropogenic ( $\beta_{Ant}$ ) scaling coefficients, as  
259 described in Tett et al. (2002):

$$260 \quad \beta_{Nat} = \beta_1 + \beta_2 \quad , \quad (2)$$

$$261 \quad \beta_{Ant} = \beta_2 \quad , \quad (3)$$

262 We construct the 5-95% confidence intervals accounting for uncertainty in the internal variability  
263 of  $\beta_{Nat}$  and  $\beta_{Ant}$  by adding 16,000 random  $L$ -year samples from the control simulations onto the  
264 noise-reduced fingerprints and observations. For each iteration, we select 3 segments without  
265 replacement from the 42 non-overlapping 132-year segments available from the 10 control  
266 simulations corresponding to the fingerprints (**Table 1**), taking 3-year means (and excluding  
267 endpoints). The best-estimate coefficients and 5–95% confidence intervals are shown in **Table**  
268 **2a**. Anthropogenic forcing is detected at the 5% one-sided significance level, whereas natural  
269 forcing is not significantly detectable. The best-estimate values of  $\beta_{Ant}$  greater than the  
270 multimodel mean (scaling of 1) suggest a larger response to anthropogenic forcing in  
271 observations than in models, particularly for ERSSTv5 where the multimodel mean is outside the  
272 5–95% uncertainty range.

273

#### 274 4.2 Forced and unforced components of the interhemispheric SST contrast

275 The best-estimate 3-year mean noise-reduced, or forced, component of  $y$ ,  $\tilde{y}$ , is shown for  
276 HadSST3 in **Figure 3b** and ERSSTv5 in **Figure 3c**, with the 5%-95% confidence intervals  
277 constructed from the 16,000 random samples from the control runs. The anthropogenic and  
278 natural contributions to the forced components are also shown; the anthropogenic component is  
279 calculated by subtracting historicalNat from historical component; see **Equations (2)-(3)**. The  
280 anthropogenic component dominates the forced response for both datasets. The forced signal  
281 consists of a negative trend to around 1980 followed by a partial recovery. The negative trend is  
282 overlaid with an increase from around 1920 to 1950.

283 The best-estimate unforced residual or effective residual time series is estimated as follows:

285 
$$\hat{\varepsilon}_{obs} = \frac{(y - \beta_1 X_{historicalNat} - \beta_2 X_{historical})}{\sqrt{1 + \beta_1^2/n + \beta_2^2/n}}$$

284 , (4)

286 where the scaling factor in the denominator is applied to account for the small component of  
 287 internal variability in the fingerprints (Schurer et al. 2015). We use both  $\beta_1$  and  $\beta_2$  in **Equation**  
 288 **(4)** since physically we expect some contribution from both natural and anthropogenic forcing  
 289 types of forcing, even though natural forcing is not found to be significant. The best-estimate  
 290 residual time series (**Figure 3d**) has prominent north-south maxima in the 1930s and mid 1960s,  
 291 with the latter followed by a rapid north-south decrease to the early 1970s. We will further  
 292 examine these decadal changes in **Section 6**.

293 **Figure 3e** shows the best-estimate residual standard deviations along with those of the  
 294 control segments (shown in purple). The best-estimate observational residuals are within the  
 295 control simulation range, suggesting consistency in magnitude between the internal variability of  
 296 the observations and the models. For example, the GISS-E2-H control simulation variability is  
 297 more consistent in magnitude to the observational residuals than the GISS-E2-H historical  
 298 variability compared to observations (**Figure 1d**). Also shown are the best-estimate residuals  
 299 estimated from applying the detection and attribution methodology to each historical realization,  
 300 described in the **Appendix** (shown in black). Note that this estimate of the internal variability  
 301 includes an unknown forced component of each model which differs from the multimodel mean  
 302 fingerprint. However, the historical best-estimate residual variability is also within the range of  
 303 the control simulations (with both larger and smaller magnitudes), indicating that the multimodel  
 304 mean fingerprints reasonably capture much of the forced variability in the individual models.

305

## 306 **5. Northern and southern components of the interhemispheric SST contrast**

307 Building on the previous section, we apply a detection and attribution analysis to NH and SH  
308 SST separately. The NH and SH fingerprints and observations are shown in **Figures 4a–4b**. Both  
309 hemisphere observations show a long-term positive trend after cooling from 1881 to around  
310 1910. NH SST shows strong warming from around 1910–1940, described as early 20<sup>th</sup> century  
311 warming (Hegerl et al., 2018), followed by a slight decrease to around 1980, then strong  
312 warming until 2012. SH SST has a short-term increase around WWII, followed by relatively  
313 steady warming. ERSSTv5 and HadSST3 have the largest overall differences following WWII in  
314 the SH, with ERSSTv5 lower by about 0.2°C in the early 1950s (**Figure 4b**), potentially related  
315 to differences in bias corrections for the transition from bucket to engine room intakes (Kennedy  
316 2014; Huang et al. 2017).

317 Using the methodology described in **Section 4.1**, we obtain the best-estimate scaling  
318 coefficients and 5–95% confidence intervals, shown in **Table 2b**. Note that our NH and SH  
319 detection and attribution analysis differs from some studies in which different indices or regions  
320 are combined when calculating scaling coefficients, such as Schurer et al. (2018). We choose this  
321 approach to extract the maximum forced variability in each hemisphere, though this allows for  
322 different scaling factors across the equator.

323 Anthropogenic forcing is detected at the 5% one-sided significance level in both the NH and  
324 SH. Natural forcing is detected in both hemispheres for HadSST3 (with  $\beta_{Nat} < 1$ ), but not in  
325 ERSSTv5. In both datasets, the best-estimate values of  $\beta_{Ant}$  are greater than 1 for both  
326 hemispheres, with the multimodel mean outside the 5–95% range for the SH. The best-estimate  
327 hemispheric forced components (**Figures 4c–4d**) are dominated by an upward trend from GHG



328 forcing, with aerosol-related NH cooling from 1950-1970 (Wilcox et al., 2013; Allen et al.,  
329 2015; Undorf et al., 2018).

330 The best-estimate residual NH and SH time series,  $\hat{\epsilon}_{obs\_NH}$  and  $\hat{\epsilon}_{obs\_SH}$ , are calculated  
331 similarly to **Equation (4) (Figures 4e-4f)**. As expected, the best-estimate residual  
332 interhemispheric SST contrast,  $\hat{\epsilon}_{obs}$  from **Equation (4)**, is very strongly correlated with the  
333 difference of  $\hat{\epsilon}_{obs\_NH}$  and  $\hat{\epsilon}_{obs\_SH}$  (HadSST3:  $r=0.98$ ; ERSSTv5:  $r=0.93$ ). The observed cooling  
334 from 1881 to around 1910 is present in both  $\hat{\epsilon}_{obs\_NH}$  and  $\hat{\epsilon}_{obs\_SH}$ ; likewise, much of the early 20<sup>th</sup>  
335 century NH warming, as  $\hat{\epsilon}_{obs\_NH}$  warms relatively steadily from 1910-1940 and later undergoes a  
336 decrease in the late 1960s.  $\hat{\epsilon}_{obs\_SH}$  increases rapidly in the late 1930s, then drops in the 1940s  
337 followed by decadal-scale variations, with minima in the mid-1960s and after the early 2000s.  
338 Both  $\hat{\epsilon}_{obs\_NH}$  and  $\hat{\epsilon}_{obs\_SH}$  have large standard deviations compared to the control simulations  
339 and the best-estimate NH and SH historical residuals (calculated following the **Appendix**;  
340 **Figure 4g**).  $\hat{\epsilon}_{obs\_NH}$  and  $\hat{\epsilon}_{obs\_SH}$  are also more positively correlated (HadSST3:  $r=0.63$ ;  
341 ERSSTv5:  $r=0.62$ ) than any of the control segments or historical residuals (**Figure 4h**). [This is  
342 not the case for the direct NH and SH SST observations, whose standard deviations and  
343 correlation are within the range of the historical realizations (not shown)]. The strong amplitude  
344 and correlation of the observed NH and SH best-estimate residuals suggest that the effect of  
345 forcing has been incompletely removed using the multimodel mean regression. The discrepancy  
346 may also be partly due to errors in observations or incorrect climate model decadal variability.

347

## 348 **6. Decadal shifts in the interhemispheric SST contrast**

349 In this section, we examine decadal shifts in the interhemispheric SST contrast. Several  
350 methodologies for identifying climate shifts exist (Overland et al., 2008). Here, we examine

351 running linear trends (Trottini et al., 2015), which have been typically used to quantify the early-  
352 2000s global mean surface temperature slowdown (Meehl et al. 2011; Schurer et al. 2015;  
353 Marotzke and Forster 2015; Medhaug et al. 2017). As our focus is on decadal-scale shifts, we  
354 examine 9-year running OLS trends applied to the 3-year running mean time series. Similar  
355 results are obtained using running trend lengths of 7 to 13 years (not shown).

356

### 357 6.1 1970 and 1920s shifts

358 **Figure 5a** shows the 3-year mean interhemispheric SST contrast along with the respective 9-  
359 year running trends. In both observational datasets, the largest-magnitude trend is the rapid drop  
360 centered around 1970, consistent with previous qualitative identification (Dima and Lohmann,  
361 2010; Thompson et al., 2010) (HadSST3: 1965–1973:  $-0.63^{\circ}\text{C}$  per decade, 1966–1974:  $-0.61^{\circ}\text{C}$   
362 per decade; ERSSTv5: 1965–1973:  $-0.60^{\circ}\text{C}$  per decade, 1966–1974:  $-0.64^{\circ}\text{C}$  per decade).  
363 Hereafter, we focus on the 1966–1974 trends in both datasets for simplicity of comparison. Both  
364 NH cooling and SH warming contribute comparable magnitudes to the 1966–1974 shift (**Table**  
365 **3**). The most positive observational NH-SH trend is centered in 1922 (1918–1926) in both  
366 datasets, also with contributions from both hemispheres (**Table 3**).

367 Though the CMIP5 historical ensemble mean interhemispheric SST contrast has a negative  
368 trend in the 1960s and 1970s, the 1966–1974 trend magnitude is less than 10% of that in the  
369 observations ( $-0.051^{\circ}\text{C}$  per decade), suggesting only a modest role of forcing in the observed  
370 trend. As shown in **Figure 5c**, the 1966–1974 observational trends are larger than any of the 36  
371 historical realizations over this period. The 1918–1926 observational interhemispheric SST  
372 trends are also much larger than the CMIP5 historical ensemble mean ( $0.008^{\circ}\text{C}$  per decade), but  
373 not as far outside the distribution of the 36 individual realizations as the 1970 shift (**Figure 5b**).

374 The observational spatial SST trends are shown for the two periods in **Figures 5d-5g**. The  
375 1966–1974 trends (**Figures 5e and 5g**) have a prominent north–south SST dipole pattern in the  
376 Atlantic, with pronounced cooling in the subpolar North Atlantic and warming in the  
377 extratropical South Atlantic, extending to the other mid-latitude basins. There is also strong  
378 cooling in the central equatorial and northeast Pacific, and a warming in the northwest Atlantic  
379 offshore the northeast US. The 1918–1926 trends (**Figures 5d and 5f**) have pronounced cooling  
380 from 35°–50°S in the Atlantic and Indian sectors. There is strong warming in the equatorial  
381 Atlantic, Labrador Sea, the northeast Pacific, and the northern Nordic and Barents seas (where  
382 not masked in ERSSTv5). The spatial trend patterns are very similar if the historical multimodel  
383 mean SST is regressed out at each gridbox (not shown).

384

## 385 6.2 Forced and unforced contributions to the 1970 and 1920s shifts

386 We examine the contributions of forced and unforced variability to the 1970 and 1920s  
387 shifts, based on the detection and attribution best-estimate residuals from **Section 4. Figure 6a**  
388 shows  $\hat{\epsilon}_{obs}$  (from **Figure 3d**) and their 9-year running trends. The 1966–1974 shift remains the  
389 most prominent in both best-estimate residuals, corresponding to 87% and 77% of the respective  
390 magnitudes of the trends in HadSST3 and ERSSTv5 respectively (**Table 3**). The 1918–1926  
391 interhemispheric trend remains nearly the same magnitude in the best-estimate residual  
392 HadSST3 as the full dataset (94% unforced), but is more reduced in ERSSTv5 (71% unforced).

393 We also examine the  $\hat{\epsilon}_{obs\_NH}$  (**Figure 6b**) and  $\hat{\epsilon}_{obs\_SH}$  (**Figure 6c**) contributions to the  
394 interhemispheric SST shifts. Both shifts result from additive trends of the NH and SH best-  
395 estimate residuals: NH cooling plus SH warming from 1966–1974; and NH warming plus SH  
396 cooling from 1918–1926.  $\hat{\epsilon}_{obs\_NH}$  has pronounced cooling trends over 1966-1974 (**Table 3**), with

397 the largest magnitude 9-year trend over the entire record for HadSST3, and the second-largest in  
398 ERSSTv5 after cooling around 1900;  $\hat{\epsilon}_{obs\_SH}$  also has large warming over this period in  
399 ERSSTv5. Warming in  $\hat{\epsilon}_{obs\_NH}$  and cooling in  $\hat{\epsilon}_{obs\_SH}$  also interfere constructively to produce  
400 the 1918–1926 interhemispheric SST trend.

401 **Figure 7a** compares the 1966–1974 trends in observations and best-estimate residuals  $\hat{\epsilon}_{obs}$   
402 with the largest-magnitude negative (SH–NH) 9-year interhemispheric SST trends in each of the  
403 non-overlapping 132-year control segments. The 1966–1974 observed interhemispheric SST  
404 trends (solid lines) exceed all trends from the control simulations; however, the reduced-  
405 magnitude  $\hat{\epsilon}_{obs}$  trends (dashed lines) are comparable to some of the largest-magnitude control  
406 trends. The largest-magnitude negative segments are found in HadGEM2-ES, CSIRO-Mk3-6-0,  
407 IPSL-CM5A-LR, and GFDL-CM3, which are among the high-standard-deviation models in  
408 **Figure 3e**. [Several control segments exceed the 1918–1926 observational and  $\hat{\epsilon}_{obs}$  trend  
409 magnitudes (not shown)].

410 **Figures 7b–7f** show the spatial patterns associated with the 5 largest-magnitude negative  
411 interhemispheric SST trends in the control simulations indicated in **Figure 7a**. The trends have  
412 general agreement with an interhemispheric dipole in the in the tropical and subtropical Atlantic,  
413 with cooling in the NH and warming in the SH. HadGEM2-ES years 114–122 (**Figure 7d**) and  
414 GFDL-CM3 years 14–22 (**Figure 7f**) show strong subpolar Atlantic cooling with warming  
415 extending off the northeast US, and GFDL-CM3 years 14–22 also shows prominent subpolar SH  
416 warming in the Weddell Sea region. In contrast, IPSL-CM5A-LR years 608–616 has subpolar  
417 North Atlantic warming south of Greenland (**Figure 7c**). CSIRO-Mk3-6-0 years 310–318  
418 (**Figure 7b**) and HadGEM2-ES years 364–372 (**Figure 7e**) have a horseshoe-pattern of mid-  
419 latitude cooling associated with North Atlantic SST variability (Gastineau and Frankignoul,

420 2015) but are less prominent in the central subpolar region. In the Pacific, CSIRO-Mk3-6-0 years  
421 310–318 (**Fig. 7b**) shows a triangle-shaped pattern resembling the transition to the negative  
422 phase of the Pacific Decadal Oscillation (PDO) / Interdecadal Pacific Oscillation (IPO) (Zhang et  
423 al. 1997; Mantua et al. 1997; Power et al. 1999), with the other model episodes generally  
424 showing the opposite phase.

425

## 426 **7. Summary and discussion**

427

### 428 7.1 Summary

429 In this study, we quantify the variability of the interhemispheric SST contrast, motivated by  
430 its importance for tropical rainfall. We examine the variability of the 3-year mean  
431 interhemispheric SST contrast from 1881 to 2012 in the HadSST3 and ERSSTv5 datasets,  
432 applying a detection and attribution analysis using multimodel mean fingerprints from 36 total  
433 realizations of 10 CMIP5 models to identify the contributions from natural and anthropogenic  
434 forcing. We also investigate the constituent northern hemisphere (NH) and southern hemisphere  
435 (SH) SST variability. Our key findings include the following:

436 (a) The temporal magnitude of observed interhemispheric SST variability is within the range  
437 of the historical CMIP5 simulations examined. The observed spatial pattern of the  
438 interhemispheric SST contrast projects most strongly over the subpolar North Atlantic and the  
439 extratropical South Atlantic and Indian oceans. The historical model mean spatial pattern also  
440 has strong amplitudes over the extratropical South Atlantic and Indian oceans, but is much  
441 stronger over the North Pacific than the North Atlantic. The tropical rainbands shift toward the

442 relatively warmer SST hemisphere in both observations and models, though most models  
443 underestimate the precipitation response over northern tropical land regions.

444 (b) Anthropogenic, but not natural forcing, is detected at the 95% significance level in the  
445 interhemispheric SST contrast. The anthropogenic scaling factors are consistent with the  
446 multimodel mean in HadSST3, but results with ERSSTv5 suggest a larger interhemispheric SST  
447 response to forcing than simulated in the multimodel mean. We find a significantly larger  
448 amplitude of the anthropogenic influence on SH SST than the multimodel mean in both datasets.  
449 Natural forcing is detected ( $p < 0.05$ ) in the NH and SH in HadSST3 only.

450 (c) After removing the multimodel mean forced signal, the best-estimate residual unforced  
451 interhemispheric SST variability is largely consistent in magnitude with that of the control  
452 simulations and best-estimate residual historical simulations. However, the best-estimate residual  
453 individual NH and SH SST have relatively larger-magnitude variability and are more positively  
454 correlated than in any of the control simulations examined.

455 (d) Using 9-year running trends, we determine that the NH–SH interhemispheric decrease  
456 around 1970 is the most prominent shift over the instrumental period, corroborating previous  
457 identification (Baines and Folland, 2007; Dima and Lohmann, 2010; Thompson et al., 2010).  
458 Based on the multimodel mean detection and attribution analysis, we find that the shift was  
459 largely unforced, and due to both unforced NH cooling and SH warming. Interhemispheric SST  
460 shifts of comparable magnitude as the best-estimate residual 1970 shift are found in the control  
461 simulations of some of the high-variability models (CSIRO-Mk3-6-0, IPSL-CM5A-LR,  
462 HadGEM2-ES, and GFDL-CM3).

463

464 7.2 Discussion

465 Here, we consider some potential caveats and issues raised by our analysis. In the same way  
466 that the early 21<sup>st</sup> century global mean surface temperature slowdown motivated further research  
467 into the global energy balance and ocean heat content (Xie, 2016; Yan et al., 2016; Medhaug et  
468 al., 2017), we hope that examination of interhemispheric SST variability can underlie future  
469 mechanistic insights.

470

### 471 *7.2.1 Fingerprint uncertainties*

472 One caveat is that we do not consider inter-model differences in the multimodel mean  
473 fingerprints in our detection and attribution framework, which would add to the scaling factor  
474 uncertainties (Hannart et al., 2014; Schurer et al., 2018). First, there is inter-model spread in the  
475 GHG-only response, which may be due to non-CO<sub>2</sub> forcings as well as different feedbacks  
476 (Jones et al. 2016). **Figure 8a** shows the 3-year mean interhemispheric SST contrast anomaly  
477 time series in 35 historical GHG-only (historicalGHG) realizations (all historical realizations in  
478 **Table 1** except for IPSL-CM5A-MR). The multimodel mean time series has a positive 1881-  
479 2012 trend of  $0.10 \pm 0.02$  °C per 100 years (slope  $\pm 2$  adjusted standard errors, widened by a factor  
480 of  $\sqrt{3}$  as described in **Section 3**). There are still considerable differences among the individual  
481 model mean trends, which provide an estimate of the range of the forced response: from –  
482  $0.04 \pm 0.04$  °C per 100 years in CSIRO-Mk3-6-0 to  $0.31 \pm 0.05$  °C per 100 years in IPSL-CM5A-  
483 LR (**Figure 8b**). [Model mean trends are calculated for the 7 models with more than 1  
484 realization]. The spread of individual realizations is wider, from  $-0.21$  to  $0.38$  °C per 100 years,  
485 as it includes a larger contribution of model internal variability (with each realization combining  
486 forced and internal variability comparable to the actual climate). We compare the 1881-2012  
487 historicalGHG interhemispheric SST trends with those of global mean SST (including gridpoints

488 from 5°S–5°N) for each realization in **Figure 8c**. The trends are strongly positively correlated  
489 ( $r=0.58$ ), suggesting that the interhemispheric SST contrast scales with global mean SST in the  
490 GHG-forced response.

491 Anthropogenic aerosol forcing also remains a large uncertainty in the multimodel mean  
492 anthropogenic fingerprint. Though all models examined except bcc-csm1-1 do contain some  
493 representation of sulfate aerosol indirect effects, inter-model differences in aerosol  
494 parameterization result in different magnitudes and spatial patterns of aerosol forcing (Ekman,  
495 2014; Guo et al., 2015; Allen et al., 2015; Rotstayn et al., 2015), particularly related to aerosol-  
496 cloud interactions (Chung and Soden, 2017). As only a subset of the CMIP5 modeling groups  
497 archived specific-forced historical anthropogenic-aerosol-only (historicalAA) realizations, we  
498 approximate the historicalAA interhemispheric contrast anomaly by subtracting the respective  
499 historicalGHG and historicalNat interhemispheric SST contrast time series from the historical  
500 interhemispheric SST contrast for each of the 35 realizations with historicalGHG output (**Figure**  
501 **8d**). Note that the internal variability of the approximate historicalAA time series will typically  
502 be larger than for an individual experiment due to it being derived from multiple experiments  
503 (historical–historicalGHG–historicalNat), which contributes to some of the inter-model spread.

504 For a sense of the magnitude of the aerosol response, we examine the interhemispheric SST  
505 contrast during the mid-20<sup>th</sup> century period of maximum interhemispheric aerosol forcing  
506 (Rotstayn and Lohmann, 2002; Hwang et al., 2013; Wilcox et al., 2013), using the 1950-1985  
507 trend as in Allen et al. (2015), shown in **Figure 8e**. The ensemble mean time series has a  
508 significant trend of  $-0.068 \pm 0.014$  °C per decade (slope  $\pm 2$  adjusted standard errors), and the  
509 model mean trends range from  $-0.16 \pm 0.04$  °C per decade in HadGEM2-ES to  $-0.012 \pm 0.032$  °C  
510 per decade in CNRM-CM5. For comparison, the observed trends over this period are  $-0.11 \pm 0.05$



511 and  $-0.16 \pm 0.039$  °C per decade in HadSST3 and ERSSTv5 respectively. Improvements in  
512 spatiotemporal aerosol emission patterns and better treatment of aerosol probabilities may reduce  
513 some of the uncertainties (Schurer et al., 2018; Haustein et al., 2019). Another partially-  
514 anthropogenic influence on the interhemispheric SST contrast is African dust emissions from  
515 land use change, which are poorly simulated by CMIP5 models (Evan et al., 2014; Allen et al.,  
516 2015).

517 Detection of natural forcing in the HadSST3 (which not being infilled is generally preferred  
518 for attribution) individual hemispheres, yet not the interhemispheric SST contrast, suggests that  
519 natural forcing over the 20<sup>th</sup> century does not show a pronounced enough hemispheric SST  
520 contrast to be detectible, despite some hemispheric asymmetry in volcanic forcing (Haywood et  
521 al., 2013; Iles and Hegerl, 2014). Recent studies increasingly show a volcanic influence on large-  
522 scale climate modes, including the AMOC, but the responses may not be well-represented across  
523 models due to their complex lagged processes and limited eruption observations over the  
524 historical period (Swingedouw et al., 2017). For instance, the 1963 Agung eruption may have  
525 forced part of the North Atlantic cooling that contributed to the interhemispheric shift around  
526 1970 (Swingedouw et al., 2013; Hodson et al., 2014). Some observational analyses also suggest  
527 that solar variability may modulate the interhemispheric SST contrast (Rajesh and Tiwari, 2018),  
528 though detection and attribution studies have so far not found a significant solar influence on  
529 large-scale surface temperatures (Schurer et al. 2014).

530

### 531 *7.2.2 Spatial and basin interhemispheric SST variability*

532 While the basic time series diagnostics (**Figures 1c-1d**) suggest that the CMIP5 models  
533 effectively reproduce the temporal characteristics of the interhemispheric SST contrast,

534 comparison of the observed (**Figures 2a and 2c**) and model mean (**Figure 2e**) spatial patterns  
535 points to some differences in the mechanisms involved. In particular, the model-mean spatial  
536 pattern has much stronger positive slopes over the North Pacific, whereas the observations have  
537 the most pronounced positive amplitudes over the subpolar North Atlantic. However, we note  
538 that the relatively short observational record and uneven SST observational data distribution,  
539 with much more data from the North Atlantic, makes it difficult to evaluate the significance of  
540 these spatial pattern differences.

541 Examination of intra-model interhemispheric SST pattern variability suggests that the  
542 extratropical North Atlantic may be more important than suggested by the multimodel mean  
543 pattern. **Figure 9** shows the ensemble standard deviation of the 36 CMIP5 historical SST  
544 regression slopes averaged in **Figure 2e**. The large inter-model variability over the extratropical  
545 North Atlantic north of 40°N contrasts with the weak model-mean slopes in this region in **Figure**  
546 **2e**, suggesting that the different patterns cancel out in the multimodel mean.

547 There are similar questions about the importance of different ocean basins in the large-  
548 magnitude interhemispheric SST shifts. The spatial patterns of the 1920s and 1970  
549 interhemispheric SST shifts (**Figures 5d-5g**) could result from linked ocean basin SST  
550 variability, as proposed between Atlantic and Pacific SST (Zhang and Delworth 2007; Chafik et  
551 al. 2016). On the other hand, the different ocean basins may be independent, as Goosse (2017)  
552 cautions that interhemispheric SST shifts can result from the superposition of unrelated  
553 processes. Among the control shifts, the sign difference in the eastern Pacific in CSIRO-Mk3-6-0  
554 years 310–318 suggests different representations linking Pacific and Atlantic SST variability, or  
555 possibly that that IPO-related Pacific variability is not important for the interhemispheric SST  
556 contrast as it extends into both hemispheres. The eastern Pacific is much less prominent in the

557 observed shifts than in the large-magnitude control shifts, though the 1970 shift does show  
558 strong central and northeast Pacific SST cooling extending to southwest North America.

559 Next, we discuss the subpolar North Atlantic and potential AMOC contribution to  
560 interhemispheric SST shifts. The mechanism of cross-equator ocean heat transport via the  
561 AMOC is thought to explain the interhemispheric “bipolar seesaw” SST pattern in glacial-  
562 interglacial paleoclimate records (Crowley, 1992; Broecker, 1998) and has been found in many  
563 modeling experiments (Vellinga and Wu, 2004; Latif et al., 2006; Stouffer et al., 2007; Sun et  
564 al., 2013, 2018). Some studies have thus used the interhemispheric SST contrast as a proxy for  
565 the AMOC (e.g. Dima and Lohmann, 2010), though the Atlantic interhemispheric SST pattern  
566 has been found to be a weaker AMOC indicator than North Atlantic SST in most CMIP5 models  
567 (Muir and Fedorov, 2015)

568 An observational limitation is that continuous direct measurements of the AMOC only began  
569 in 2004 (with altimetry extending the record to 1993), which is not nearly long enough to resolve  
570 decadal and multidecadal variability. Recently, it has been proposed that the century-long SST  
571 cooling trend in the subpolar North Atlantic, sometimes referred to as the “warming hole”,  
572 indicates a long-term decrease in the AMOC over the 20<sup>th</sup> century (Drijfhout et al., 2012;  
573 Rahmstorf et al., 2015; Caesar et al., 2018), though the relationship between these surface  
574 changes and the AMOC remains contested (Josey et al., 2018). Negative trends in subpolar  
575 Atlantic surface salinity and density since the early 20<sup>th</sup> century are consistent with an AMOC  
576 decrease, though other factors could also be responsible (Friedman et al., 2017; Reverdin et al.,  
577 2019). Oceanographic proxy reconstructions also suggest a longer-term AMOC decline since the  
578 end of the Little Ice Age (Thibodeau et al., 2018; Thornalley et al., 2018).

579 As an indirect index of the AMOC, we calculate an AMOC proxy SST time series following  
580 Rahmstorf et al. (2015) and Caesar et al. (2018) as the difference of the North Atlantic subpolar  
581 gyre (SPG; 50°–15°W, 50°–60°N) and global mean SST, using 3-year running annual means and  
582 masked as shown in **Figure 1b**. First, we briefly examine the long-term GHG-forced trends of  
583 the AMOC proxy SST index. The 1881–2012 historicalGHG multimodel mean trend of the  
584 AMOC proxy SST index (of the models examined in **Figures 8a-8c**) is  $-0.50 \pm 0.07$  °C per 100  
585 years (slope $\pm 2$  adjusted standard errors), consistent with the GHG-forced AMOC slowdown  
586 simulated by the models (Caesar et al., 2018). We find that the 1881–2012 AMOC proxy SST  
587 index trends are very strongly correlated with the respective interhemispheric SST trends across  
588 the historicalGHG simulations ( $r=0.77$ ).

589 Next, we examine the observed and historical SST AMOC proxy time series variability.  
590 **Figure 10a** shows the observed interhemispheric SST contrast and 3-year mean SST AMOC  
591 proxy time series anomalies. Though they are strongly correlated (HadSST3:  $r=0.63$ ; ERSSTv5:  
592  $r=0.58$ ), the AMOC proxy SST time series shows stronger variability on longer decadal  
593 timescales, and the interhemispheric SST contrast lacks the long-term 20<sup>th</sup> century trend in the  
594 AMOC proxy SST time series. **Figure 10b** compares the observed correlations of the  
595 interhemispheric SST contrast and the AMOC SST proxy index with the historical models. The  
596 observed correlations are stronger than nearly all of the historical realizations, with some models  
597 showing zero or negative correlations. This is consistent with the discrepancy between **Figure 2e**  
598 and **Figures 2a** and **2c**, indicating that the Atlantic SPG plays a much larger role in the observed  
599 interhemispheric SST contrast than in most models. This suggests that many models could be  
600 misrepresenting some processes of Atlantic interhemispheric SST variability related to the  
601 AMOC, or a common response to forcings.

602 Looking forward, simulation of Atlantic interhemispheric SST variability may improve with  
603 increasing model resolution. For example, Hutchinson et al. (2015) find a larger interhemispheric  
604 temperature response in an Atlantic-sector coupled climate model using an eddy-permitting 0.25°  
605 ocean resolution compared to a 1° resolution which is typical of CMIP5 models. North Atlantic  
606 decadal variability may also improve with correction of North Atlantic mean state biases,  
607 particularly salinity, related to AMOC variability (Menary et al., 2015; Park et al., 2016; Liu et  
608 al., 2017).

609 A related question is the role of the AMOC in the interhemispheric SST shifts in the 1920s  
610 and around 1970. The AMOC proxy SST time series of **Figure 10a** shows a rapid drop during  
611 the 1970 shift, though not as prominent in the overall record given the larger decadal variability.  
612 The spatial SST pattern associated with the 1970 shift (**Figures 5e** and **5g**) shows an Atlantic  
613 interhemispheric SST dipole suggested as an AMOC fingerprint (e.g. (Dima and Lohmann,  
614 2010)) as well as the specific AMOC slowdown pattern of subpolar Atlantic cooling and  
615 warming offshore the northeast United States (Saba et al., 2016; Caesar et al., 2018). Subsurface  
616 salinity and temperature profiles also suggest an AMOC decline during the mid-20<sup>th</sup> century  
617 concurrent with the interhemispheric SST shift around 1970 (Hodson et al., 2014). However,  
618 determining the role of the AMOC from alternative mechanisms is difficult on such short  
619 timescales given the lack of data over the period. For example, Wang et al. (2015) showed that  
620 atmospheric teleconnections can also produce an interhemispheric Atlantic SST dipole pattern.  
621 In contrast, the 1920s do not have a persistent increase in the AMOC proxy SST record in  
622 **Figure 10a**, but rather strong inter-annual variability. Likewise, the spatial SST pattern  
623 associated with the 1920s shift (**Figures 5d** and **5f**) does not have an Atlantic interhemispheric  
624 dipole; the sign change is around 30°S rather than in the equatorial Atlantic.

625 Decadal shifts in the subpolar North Atlantic have previously been described in several  
626 different unforced simulations involving linkages between blocking, sea ice, and AMOC  
627 feedbacks (Drijfhout et al., 2013; Kleppin et al., 2015; Moreno-Chamarro et al., 2015; Sgubin et  
628 al., 2017). Understanding how these different processes may contribute to the interhemispheric  
629 SST shifts in the control simulations remains a topic of future investigation. Among our sample  
630 of large-magnitude events (**Figure 7b–7e**), HadGEM2-ES years 114–122 and GFDL-CM3 years  
631 14–22 show strong and coherent cooling in the subpolar North Atlantic and warming in the Gulf  
632 Stream extension, which are consistent with the spatial fingerprint of an AMOC slowdown (Saba  
633 et al., 2016; Caesar et al., 2018); GFDL-CM3 in particular has been found to have large-  
634 amplitude multidecadal AMOC variability (Cheng et al., 2013). The warming found in GFDL-  
635 CM3 years 14–22 in the high-latitude SH adjacent to Antarctica has been suggested to be an  
636 AMOC slowdown signature (Dima and Lohmann, 2010). Though the IPSL-CM5A-LR control  
637 shift in years 608–616 shows strong *warming* in the subpolar North Atlantic, this could  
638 potentially be due to the AMOC: as shown in Muir and Fedorov (2015) (their Figure 4), the  
639 IPSL-CM5A-LR AMOC SST spatial pattern has anomalies of opposing sign in the subpolar  
640 North Atlantic.

641

### 642 *7.2.3 NH and SH variability*

643 An intriguing finding from our detection and attribution analysis is that the best-estimate  
644 residual NH and SST are more positively correlated than in any of the control simulations  
645 (**Figure 4h**). Likewise, the best-estimate residual NH and SH SST standard deviations are at the  
646 upper end of the control simulation variability (**Figure 4g**), which is not the case for the  
647 interhemispheric SST contrast (**Figure 3e**). The positive best-estimate residual NH and SH SST

648 correlation and large-magnitude variability are consistent: the in-phase residual NH and SH SST  
649 variations have a canceling influence on the interhemispheric SST contrast.

650 There are a couple of possibilities that could account for the large positive best-estimate  
651 residual NH and SH SST correlation and large-magnitude variability. One explanation, related to  
652 the fingerprint uncertainties discussed in **Section 7.2.1**, is that there is a common NH and SH  
653 forced component which is missing or underestimated by the models. For example, climate  
654 models may underestimate the cooling from early 20<sup>th</sup> century eruptions, such as 1912 Katmai  
655 (1912) and Colima (1913), accounting for the early 20<sup>th</sup> century discrepancies between the NH  
656 and SH fingerprints and observations in **Figures 4a-4b**.

657 Common SST data biases in the NH and SH could also artificially inflate the correlation.  
658 Recent studies examining geographic biases (Cowtan et al. 2018; Chan and Huybers 2019) and  
659 hemispheric and global time series (Folland et al., 2018; Haustein et al., 2019) have found that  
660 WWII-era warming and potentially also some cooling around 1900 remain inflated in gridded  
661 observational data products. A third possibility is that the models may underestimate common  
662 decadal variability in the NH and SH SST. IPO-related Pacific decadal variability, which has  
663 been linked to excursions in global mean surface temperature (Kosaka and Xie, 2013; Maher et  
664 al., 2014; England et al., 2014; Dai et al., 2015; Gastineau et al., 2019), is underestimated by  
665 many CMIP5 models (Kociuba and Power, 2015; Henley et al., 2017). Pacific decadal variability  
666 may account for some of the joint negative values in residual NH and SH SST after around 2000  
667 (**Figures 4e-4f**), reflecting lower global mean SST than the CMIP5 historical model mean in the  
668 so-called *hiatus* or slowdown (Fyfe et al. 2013; Medhaug et al. 2017).

669 These discrepancies raise questions about the use of model control experiments to simulate  
670 background variability, as in many detection and attribution studies (as well as other analyses

671 such as future projections). Using control simulations with unrealistic variability means that the  
672 confidence intervals calculated in analyses using them may be over- or under-confident, which  
673 could lead to misleading conclusions. In the future, perhaps the simulation of internal variability  
674 should be treated more explicitly in model selection (e.g. Knutti et al., 2010).

675

## 676 **Acknowledgments**

677 A.R.F, G.C.H., and A.S. were supported by the ERC-funded TITAN project (EC-320691).  
678 A.R.F. was also supported by the U.S. NSF grant EAPSI-1311103 and the UK NERC-funded  
679 SMURPHs project (NE/N006143/1). G.C.H. and A.S. were further supported by the UK NERC  
680 under the Belmont forum, Grant PacMedy (NE/P006752/1). S.-Y.L. was funded by the Taiwan  
681 NSC grant 102-2611-M-001-006. J.C.H.C was supported by the U.S. DOE Office of Science,  
682 Biological and Environmental Research program (DE-FG02-08ER64588). The HadSST3 data  
683 were provided by the UK Met Office Hadley Center, and the ERSSTv5 data were provided by  
684 the U.S. NOAA's National Centers for Environmental Information. We acknowledge the World  
685 Climate Research Program's Working Group on Coupled Modeling, which is responsible for  
686 CMIP and the climate modeling groups for producing and making available their model output.  
687 For CMIP the U.S. DOE's Program for Climate Model Diagnosis and Intercomparison provides  
688 coordinating support and led development of software infrastructure in partnership with the  
689 Global Organization for Earth System Science Portals. The CMIP5 output was hosted by the UK  
690 Center for Environmental Data Analysis. We thank Debbie Polson for providing the detection  
691 and attribution code and Mike Mineter for valuable assistance. We appreciate the constructive  
692 feedback from three anonymous reviewers.

693



694 **Appendix: historical simulation residuals**

695 The best-estimate residuals are estimated for each historical realization as follows. Building  
696 on Schurer et al. (2015), we modify the denominator scaling in **Equation (4)** to account for the  
697 component of shared variance of each individual historical realization time series with the model  
698 mean fingerprint  $X_{historical}$  (the average of all historical realization time series):

699

701 
$$\hat{\epsilon}_{historical} = \frac{(\gamma_{historical} - \beta_1 X_{historicalNat} - \beta_2 X_{historical})}{\sqrt{\frac{\beta_1^2}{n} + \frac{(n - \beta_2)^2 + \beta_2^2(n - 1)}{n^2}}}$$

700 , (A1)

702 where  $\gamma_{historical}$  is the respective historical realization time series.

703

704 **References**

- 705 Allen, M.R., Stott, P.A., 2003. Estimating signal amplitudes in optimal fingerprinting, part I:  
706 theory. *Clim. Dyn.* 21, 477–491. <https://doi.org/10.1007/s00382-003-0313-9>
- 707 Allen, R.J., Evan, A.T., Booth, B.B.B., 2015. Interhemispheric Aerosol Radiative Forcing and  
708 Tropical Precipitation Shifts during the Late Twentieth Century. *J. Clim.* 28, 8219–  
709 8246. <https://doi.org/10.1175/JCLI-D-15-0148.1>
- 710 Armour, K.C., Marshall, J., Scott, J.R., Donohoe, A., Newsom, E.R., 2016. Southern Ocean  
711 warming delayed by circumpolar upwelling and equatorward transport. *Nat. Geosci.*  
712 9, 549–554. <https://doi.org/10.1038/ngeo2731>
- 713 Baines, P., Folland, C., 2007. Evidence for a rapid global climate shift across the late 1960s. *J.*  
714 *Clim.* 20, 2721–2744. <https://doi.org/10.1175/JCLI4177.1>
- 715 Becker, A., Finger, P., Meyer-Christoffer, A., Rudolf, B., Schamm, K., Schneider, U., Ziese, M.,  
716 2013. A description of the global land-surface precipitation data products of the  
717 Global Precipitation Climatology Centre with sample applications including  
718 centennial (trend) analysis from 1901–present. *Earth Syst. Sci. Data* 5, 71–99.  
719 <https://doi.org/10.5194/essd-5-71-2013>
- 720 Biasutti, M., Held, I.M., Sobel, A.H., Giannini, A., 2008. SST Forcings and Sahel Rainfall  
721 Variability in Simulations of the Twentieth and Twenty-First Centuries. *J. Clim.* 21,  
722 3471–3486.
- 723 Bindoff, N.L., Stott, P.A., AchutaRao, K.M., Allen, M.R., Gillett, N., Gutzler, D., Hansingo, K.,  
724 Hegerl, G., Hu, Y., Jain, S., Mokhov, I.I., Overland, J., Perlwitz, J., Sebbari, R., Zhang, X.,  
725 2013. Detection and Attribution of Climate Change: from Global to Regional, in:  
726 *Climate Change 2013: The Physical Science Basis. Contribution of Working Group I*  
727 *to the Fifth Assessment Report of the Intergovernmental Panel on Climate Change.*  
728 Cambridge University Press, Cambridge, pp. 867–952.
- 729 Bond, T.C., Doherty, S.J., Fahey, D.W., Forster, P.M., Berntsen, T., DeAngelo, B.J., Flanner,  
730 M.G., Ghan, S., Kärcher, B., Koch, D., Kinne, S., Kondo, Y., Quinn, P.K., Sarofim, M.C.,  
731 Schultz, M.G., Schulz, M., Venkataraman, C., Zhang, H., Zhang, S., Bellouin, N.,  
732 Guttikunda, S.K., Hopke, P.K., Jacobson, M.Z., Kaiser, J.W., Klimont, Z., Lohmann, U.,  
733 Schwarz, J.P., Shindell, D., Storelvmo, T., Warren, S.G., Zender, C.S., 2013. Bounding  
734 the role of black carbon in the climate system: A scientific assessment. *J. Geophys.*  
735 *Res. Atmospheres* 118, 5380–5552. <https://doi.org/10.1002/jgrd.50171>
- 736 Booth, B.B.B., Harris, G.R., Jones, A., Wilcox, L., Hawcroft, M., Carslaw, K.S., 2018. Comments  
737 on “Rethinking the Lower Bound on Aerosol Radiative Forcing.” *J. Clim.* 31, 9407–  
738 9412. <https://doi.org/10.1175/JCLI-D-17-0369.1>
- 739 Boucher, O., Randall, D., Artaxo, P., Bretherton, C., Feingold, G., Forster, P., Kerminen, V.-M.,  
740 Kondo, Y., Liao, H., Lohmann, U., 2013. Clouds and aerosols, in: *Climate Change 2013:*  
741 *The Physical Science Basis. Contribution of Working Group I to the Fifth Assessment*  
742 *Report of the Intergovernmental Panel on Climate Change.* Cambridge University  
743 Press, pp. 571–657.
- 744 Broecker, W.S., 1998. Paleocean circulation during the Last Deglaciation: A bipolar seesaw?  
745 *Paleoceanography* 13, 119–121. <https://doi.org/10.1029/97PA03707>
- 746 Caesar, L., Rahmstorf, S., Robinson, A., Feulner, G., Saba, V., 2018. Observed fingerprint of a  
747 weakening Atlantic Ocean overturning circulation. *Nature* 556, 191–196.  
748 <https://doi.org/10.1038/s41586-018-0006-5>

749 Chafik, L., Häkkinen, S., England, M.H., Carton, J.A., Nigam, S., Ruiz-Barradas, A., Hannachi, A.,  
750 Miller, L., 2016. Global linkages originating from decadal oceanic variability in the  
751 subpolar North Atlantic. *Geophys. Res. Lett.* 43, 2016GL071134.  
752 <https://doi.org/10.1002/2016GL071134>

753 Chan, D., Huybers, P., 2019. Systematic Differences in Bucket Sea Surface Temperature  
754 Measurements among Nations Identified Using a Linear-Mixed-Effect Method. *J.*  
755 *Clim.* 32, 2569–2589. <https://doi.org/10.1175/JCLI-D-18-0562.1>

756 Chang, C.-Y., Chiang, J.C.H., Wehner, M.F., Friedman, A.R., Ruedy, R., 2011. Sulfate aerosol  
757 control of Tropical Atlantic climate over the Twentieth Century. *J. Clim.*  
758 110301125651015. <https://doi.org/10.1175/2010JCLI4065.1>

759 Cheng, W., Chiang, J.C.H., Zhang, D., 2013. Atlantic Meridional Overturning Circulation  
760 (AMOC) in CMIP5 Models: RCP and Historical Simulations. *J. Clim.* 26, 7187–7197.  
761 <https://doi.org/10.1175/JCLI-D-12-00496.1>

762 Chiang, J.C.H., Friedman, A.R., 2012. Extratropical Cooling, Interhemispheric Thermal  
763 Gradients, and Tropical Climate Change. *Annu. Rev. Earth Planet. Sci.* 40, 383–412.  
764 <https://doi.org/10.1146/annurev-earth-042711-105545>

765 Chung, C., Ramanathan, V., 2007. Relationship between trends in land precipitation and  
766 tropical SST gradient. *Geophys. Res. Lett.* 34.  
767 <https://doi.org/10.1029/2007GL030491>

768 Chung, E.-S., Soden, B.J., 2017. Hemispheric climate shifts driven by anthropogenic aerosol-  
769 cloud interactions. *Nat. Geosci.* 10, 566–571. <https://doi.org/10.1038/ngeo2988>

770 Cowtan, K., Rohde, R., Hausfather, Z., 2018. Evaluating biases in sea surface temperature  
771 records using coastal weather stations. *Q. J. R. Meteorol. Soc.* 144, 670–681.  
772 <https://doi.org/10.1002/qj.3235>

773 Crowley, T.J., 1992. North Atlantic Deep Water cools the southern hemisphere.  
774 *Paleoceanography* 7, 489–497. <https://doi.org/10.1029/92PA01058>

775 Dai, A., 2013. The influence of the inter-decadal Pacific oscillation on US precipitation  
776 during 1923–2010. *Clim. Dyn.* 41, 633–646. <https://doi.org/10.1007/s00382-012-1446-5>

777  
778 Dai, A., Fyfe, J.C., Xie, S.-P., Dai, X., 2015. Decadal modulation of global surface temperature  
779 by internal climate variability. *Nat. Clim. Change* 5, 555–559.  
780 <https://doi.org/10.1038/nclimate2605>

781 Dickson, R.R., Meincke, J., Malmberg, S.-A., Lee, A.J., 1988. The “great salinity anomaly” in  
782 the northern North Atlantic 1968–1982. *Prog. Oceanogr.* 20, 103–151.

783 Dima, M., Lohmann, G., 2010. Evidence for Two Distinct Modes of Large-Scale Ocean  
784 Circulation Changes over the Last Century. *J. Clim.* 23, 5–16.  
785 <https://doi.org/10.1175/2009JCLI2867.1>

786 Drijfhout, S., Gleeson, E., Dijkstra, H.A., Livina, V., 2013. Spontaneous abrupt climate change  
787 due to an atmospheric blocking–sea-ice–ocean feedback in an unforced climate  
788 model simulation. *Proc. Natl. Acad. Sci.* 110, 19713–19718.  
789 <https://doi.org/10.1073/pnas.1304912110>

790 Drijfhout, S., van Oldenborgh, G.J., Cimadoribus, A., 2012. Is a Decline of AMOC Causing the  
791 Warming Hole above the North Atlantic in Observed and Modeled Warming  
792 Patterns? *J. Clim.* 25, 8373–8379. <https://doi.org/10.1175/JCLI-D-12-00490.1>

793 Drost, F., Karoly, D., 2012. Evaluating global climate responses to different forcings using  
794 simple indices. *Geophys. Res. Lett.* 39, L16701.  
795 <https://doi.org/10.1029/2012GL052667>

796 Ekman, A.M.L., 2014. Do sophisticated parameterizations of aerosol-cloud interactions in  
797 CMIP5 models improve the representation of recent observed temperature trends?  
798 *J. Geophys. Res. Atmospheres* 119, 817–832.  
799 <https://doi.org/10.1002/2013JD020511>

800 England, M.H., McGregor, S., Spence, P., Meehl, G.A., Timmermann, A., Cai, W., Gupta, A.S.,  
801 McPhaden, M.J., Purich, A., Santoso, A., 2014. Recent intensification of wind-driven  
802 circulation in the Pacific and the ongoing warming hiatus. *Nat. Clim. Change* 4, 222–  
803 227. <https://doi.org/10.1038/nclimate2106>

804 Evan, A.T., Flamant, C., Fiedler, S., Doherty, O., 2014. An analysis of aeolian dust in climate  
805 models. *Geophys. Res. Lett.* 41, 5996–6001.  
806 <https://doi.org/10.1002/2014GL060545>

807 Feulner, G., Rahmstorf, S., Levermann, A., Volkwardt, S., 2013. On the Origin of the Surface  
808 Air Temperature Difference between the Hemispheres in Earth’s Present-Day  
809 Climate. *J. Clim.* 26, 7136–7150. <https://doi.org/10.1175/JCLI-D-12-00636.1>

810 Folland, C., Palmer, T., Parker, D., 1986. Sahel Rainfall And Worldwide Sea Temperatures,  
811 1901-85. *Nature* 320, 602–607.

812 Folland, C.K., Boucher, O., Colman, A., Parker, D.E., 2018. Causes of irregularities in trends of  
813 global mean surface temperature since the late 19th century. *Sci. Adv.* 4, eaao5297.  
814 <https://doi.org/10.1126/sciadv.aao5297>

815 Friedman, A.R., Hwang, Y.-T., Chiang, J.C.H., Frierson, D.M.W., 2013. Interhemispheric  
816 Temperature Asymmetry over the Twentieth Century and in Future Projections. *J.*  
817 *Clim.* 26, 5419–5433. <https://doi.org/10.1175/JCLI-D-12-00525.1>

818 Friedman, A.R., Reverdin, G., Khodri, M., Gastineau, G., 2017. A new record of Atlantic sea  
819 surface salinity from 1896 to 2013 reveals the signatures of climate variability and  
820 long-term trends. *Geophys. Res. Lett.* 2017GL072582.  
821 <https://doi.org/10.1002/2017GL072582>

822 Fyfe, J.C., Gillett, N.P., Zwiers, F.W., 2013. Overestimated global warming over the past 20  
823 years. *Nat. Clim. Change* 3, 767–769. <https://doi.org/10.1038/nclimate1972>

824 Gastineau, G., Frankignoul, C., 2015. Influence of the North Atlantic SST Variability on the  
825 Atmospheric Circulation during the Twentieth Century. *J. Clim.* 28, 1396–1416.  
826 <https://doi.org/10.1175/JCLI-D-14-00424.1>

827 Gastineau, G., Friedman, A.R., Khodri, M., Vialard, J., 2019. Global ocean heat content  
828 redistribution during the 1998–2012 Interdecadal Pacific Oscillation negative  
829 phase. *Clim. Dyn.* 53, 1187–1208. <https://doi.org/10.1007/s00382-018-4387-9>

830 Genovese, C.R., Lazar, N.A., Nichols, T., 2002. Thresholding of Statistical Maps in Functional  
831 Neuroimaging Using the False Discovery Rate. *NeuroImage* 15, 870–878.  
832 <https://doi.org/10.1006/nimg.2001.1037>

833 Goose, H., 2017. Reconstructed and simulated temperature asymmetry between  
834 continents in both hemispheres over the last centuries. *Clim. Dyn.* 48, 1483–1501.  
835 <https://doi.org/10.1007/s00382-016-3154-z>

836 Guo, L., Turner, A.G., Highwood, E.J., 2015. Impacts of 20th century aerosol emissions on the  
837 South Asian monsoon in the CMIP5 models. *Atmospheric Chem. Phys.* 15, 6367–  
838 6378. <https://doi.org/10.5194/acp-15-6367-2015>

839 Hannart, A., Ribes, A., Naveau, P., 2014. Optimal fingerprinting under multiple sources of  
840 uncertainty. *Geophys. Res. Lett.* 41, 1261–1268.  
841 <https://doi.org/10.1002/2013GL058653>

842 Hansen, J., Ruedy, R., Sato, M., Lo, K., 2010. Global Surface Temperature Change. *Rev.*  
843 *Geophys.* 48, 29 PP. <https://doi.org/201010.1029/2010RG000345>

844 Haustein, K., Otto, F.E.L., Venema, V., Jacobs, P., Cowtan, K., Hausfather, Z., Way, R.G., White,  
845 B., Subramanian, A., Schurer, A.P., 2019. A Limited Role for Unforced Internal  
846 Variability in Twentieth-Century Warming. *J. Clim.* 32, 4893–4917.  
847 <https://doi.org/10.1175/JCLI-D-18-0555.1>

848 Haywood, J.M., Jones, A., Bellouin, N., Stephenson, D., 2013. Asymmetric forcing from  
849 stratospheric aerosols impacts Sahelian rainfall. *Nat. Clim. Change* 3, 660–665.  
850 <https://doi.org/10.1038/nclimate1857>

851 Hegerl, G., Zwiers, F., 2011. Use of models in detection and attribution of climate change.  
852 *Wiley Interdiscip. Rev. Clim. Change* 2, 570–591. <https://doi.org/10.1002/wcc.121>

853 Hegerl, G.C., Black, E., Allan, R.P., Ingram, W.J., Polson, D., Trenberth, K.E., Chadwick, R.S.,  
854 Arkin, P.A., Sarojini, B.B., Becker, A., Dai, A., Durack, P.J., Easterling, D., Fowler, H.J.,  
855 Kendon, E.J., Huffman, G.J., Liu, C., Marsh, R., New, M., Osborn, T.J., Skliris, N., Stott,  
856 P.A., Vidale, P.-L., Wijffels, S.E., Wilcox, L.J., Willett, K.M., Zhang, X., 2015. Challenges  
857 in Quantifying Changes in the Global Water Cycle. *Bull. Am. Meteorol. Soc.* 96, 1097–  
858 1115. <https://doi.org/10.1175/BAMS-D-13-00212.1>

859 Hegerl, G.C., Brönnimann, S., Schurer, A., Cowan, T., 2018. The early 20th century warming:  
860 Anomalies, causes, and consequences. *Wiley Interdiscip. Rev. Clim. Change* 9, e522.  
861 <https://doi.org/10.1002/wcc.522>

862 Hegerl, G.C., Hasselmann, K., Cubasch, U., Mitchell, J.F.B., Roeckner, E., Voss, R., Waszkewitz,  
863 J., 1997. Multi-fingerprint detection and attribution analysis of greenhouse gas,  
864 greenhouse gas-plus-aerosol and solar forced climate change. *Clim. Dyn.* 13, 613–  
865 634. <https://doi.org/10.1007/s003820050186>

866 Henley, B.J., Meehl, G., Power, S.B., Folland, C.K., King, A.D., Brown, J.N., Karoly, D.J., Delage,  
867 F., Gallant, A.J.E., Freund, M., Neukom, R., 2017. Spatial and temporal agreement in  
868 climate model simulations of the Interdecadal Pacific Oscillation. *Environ. Res. Lett.*  
869 12, 044011. <https://doi.org/10.1088/1748-9326/aa5cc8>

870 Hodson, D.L.R., Robson, J.I., Sutton, R.T., 2014. An Anatomy of the Cooling of the North  
871 Atlantic Ocean in the 1960s and 1970s. *J. Clim.* 27, 8229–8243.  
872 <https://doi.org/10.1175/JCLI-D-14-00301.1>

873 Hoesly, R.M., Smith, S.J., Feng, L., Klimont, Z., Janssens-Maenhout, G., Pitkanen, T., Seibert,  
874 J.J., Vu, L., Andres, R.J., Bolt, R.M., Bond, T.C., Dawidowski, L., Kholod, N., Kurokawa, J.,  
875 Li, M., Liu, L., Lu, Z., Moura, M.C.P., O'Rourke, P.R., Zhang, Q., 2018. Historical (1750–  
876 2014) anthropogenic emissions of reactive gases and aerosols from the Community  
877 Emissions Data System (CEDS). *Geosci. Model Dev.* 11, 369–408.  
878 <https://doi.org/10.5194/gmd-11-369-2018>

879 Huang, B., Thorne, P.W., Banzon, V.F., Boyer, T., Chepurin, G., Lawrimore, J.H., Menne, M.J.,  
880 Smith, T.M., Vose, R.S., Zhang, H.-M., 2017. Extended Reconstructed Sea Surface  
881 Temperature, Version 5 (ERSSTv5): Upgrades, Validations, and Intercomparisons. *J.*  
882 *Clim.* 30, 8179–8205. <https://doi.org/10.1175/JCLI-D-16-0836.1>

883 Hutchinson, D.K., England, M.H., M. Hogg, A., Snow, K., 2015. Interhemispheric Asymmetry  
884 of Warming in an Eddy-Permitting Coupled Sector Model. *J. Clim.* 28, 7385–7406.  
885 <https://doi.org/10.1175/JCLI-D-15-0014.1>

886 Hutchinson, D.K., England, M.H., Santoso, A., Hogg, A.McC., 2013. Interhemispheric  
887 asymmetry in transient global warming: The role of Drake Passage. *Geophys. Res.*  
888 *Lett.* 40, 1587–1593. <https://doi.org/10.1002/grl.50341>

889 Hwang, Y.-T., Frierson, D.M.W., Kang, S.M., 2013. Anthropogenic sulfate aerosol and the  
890 southward shift of tropical precipitation in the late 20th century. *Geophys. Res. Lett.*  
891 40, 2845–2850. <https://doi.org/10.1002/grl.50502>

892 Iles, C.E., Hegerl, G.C., 2014. The global precipitation response to volcanic eruptions in the  
893 CMIP5 models. *Environ. Res. Lett.* 9. [https://doi.org/10.1088/1748-](https://doi.org/10.1088/1748-9326/9/10/104012)  
894 [9326/9/10/104012](https://doi.org/10.1088/1748-9326/9/10/104012)

895 Jones, G.S., Stott, P.A., Mitchell, J.F.B., 2016. Uncertainties in the attribution of greenhouse  
896 gas warming and implications for climate prediction. *J. Geophys. Res. Atmospheres*  
897 121, 6969–6992. <https://doi.org/10.1002/2015JD024337>

898 Josey, S.A., Hirschi, J.J.-M., Sinha, B., Duchez, A., Grist, J.P., Marsh, R., 2018. The Recent  
899 Atlantic Cold Anomaly: Causes, Consequences, and Related Phenomena. *Annu. Rev.*  
900 *Mar. Sci.* 10, 475–501. <https://doi.org/10.1146/annurev-marine-121916-063102>

901 Kang, S.M., Seager, R., Frierson, D.M.W., Liu, X., 2014. Croll revisited: Why is the northern  
902 hemisphere warmer than the southern hemisphere? *Clim. Dyn.* 44, 1457–1472.  
903 <https://doi.org/10.1007/s00382-014-2147-z>

904 Kennedy, J.J., 2014. A review of uncertainty in in situ measurements and data sets of sea  
905 surface temperature. *Rev. Geophys.* 52, 1–32.  
906 <https://doi.org/10.1002/2013RG000434>

907 Kennedy, J.J., Rayner, N.A., Smith, R.O., Parker, D.E., Saunby, M., 2011a. Reassessing biases  
908 and other uncertainties in sea surface temperature observations measured in situ  
909 since 1850: 1. Measurement and sampling uncertainties. *J. Geophys. Res.* 116, 13 PP.  
910 <https://doi.org/201110.1029/2010JD015218>

911 Kennedy, J.J., Rayner, N.A., Smith, R.O., Parker, D.E., Saunby, M., 2011b. Reassessing biases  
912 and other uncertainties in sea surface temperature observations measured in situ  
913 since 1850: 2. Biases and homogenization. *J. Geophys. Res.* 116, 22 PP.  
914 <https://doi.org/201110.1029/2010JD015220>

915 Kiehl, J.T., Briegleb, B.P., 1993. The Relative Roles Of Sulfate Aerosols And Greenhouse  
916 Gases In Climate Forcing. *Science* 260, 311–314.

917 Kleppin, H., Jochum, M., Otto-Bliesner, B., Shields, C.A., Yeager, S., 2015. Stochastic  
918 Atmospheric Forcing as a Cause of Greenland Climate Transitions. *J. Clim.* 28, 7741–  
919 7763. <https://doi.org/10.1175/JCLI-D-14-00728.1>

920 Knutti, R., Furrer, R., Tebaldi, C., Cermak, J., Meehl, G.A., 2010. Challenges in Combining  
921 Projections from Multiple Climate Models. *J. Clim.* 23, 2739–2758.  
922 <https://doi.org/10.1175/2009JCLI3361.1>

923 Kociuba, G., Power, S.B., 2015. Inability of CMIP5 Models to Simulate Recent Strengthening  
924 of the Walker Circulation: Implications for Projections. *J. Clim.* 28, 20–35.  
925 <https://doi.org/10.1175/JCLI-D-13-00752.1>

926 Kosaka, Y., Xie, S.-P., 2013. Recent global-warming hiatus tied to equatorial Pacific surface  
927 cooling. *Nature* 501, 403–407. <https://doi.org/10.1038/nature12534>

- 928 Kretzschmar, J., Salzmann, M., Mülmenstädt, J., Boucher, O., Quaas, J., 2017. Comment on  
929 “Rethinking the Lower Bound on Aerosol Radiative Forcing.” *J. Clim.* 30, 6579–6584.  
930 <https://doi.org/10.1175/JCLI-D-16-0668.1>
- 931 Lamarque, J.-F., Bond, T.C., Eyring, V., Granier, C., Heil, A., Klimont, Z., Lee, D., Lioussé, C.,  
932 Mieville, A., Owen, B., Schultz, M.G., Shindell, D., Smith, S.J., Stehfest, E., Van  
933 Aardenne, J., Cooper, O.R., Kainuma, M., Mahowald, N., McConnell, J.R., Naik, V., Riahi,  
934 K., van Vuuren, D.P., 2010. Historical (1850-2000) gridded anthropogenic and  
935 biomass burning emissions of reactive gases and aerosols: methodology and  
936 application. *Atmospheric Chem. Phys.* 10, 7017–7039. [https://doi.org/10.5194/acp-](https://doi.org/10.5194/acp-10-7017-2010)  
937 [10-7017-2010](https://doi.org/10.5194/acp-10-7017-2010)
- 938 Latif, M., Boening, C., Willebrand, J., Biastoch, A., Dengg, J., Keenlyside, N., Schweckendiek,  
939 U., Madec, G., 2006. Is the thermohaline circulation changing? *J. Clim.* 19, 4631–  
940 4637. <https://doi.org/10.1175/JCLI3876.1>
- 941 Liu, W., Xie, S.-P., Liu, Z., Zhu, J., 2017. Overlooked possibility of a collapsed Atlantic  
942 Meridional Overturning Circulation in warming climate. *Sci. Adv.* 3, e1601666.  
943 <https://doi.org/10.1126/sciadv.1601666>
- 944 Liu, Y., Chiang, J.C.H., 2012. Coordinated Abrupt Weakening of the Eurasian and North  
945 African Monsoons in the 1960s and Links to Extratropical North Atlantic Cooling. *J.*  
946 *Clim.* 25, 3532–3548. <https://doi.org/10.1175/JCLI-D-11-00219.1>
- 947 Maher, N., Gupta, A.S., England, M.H., 2014. Drivers of decadal hiatus periods in the 20th  
948 and 21st centuries. *Geophys. Res. Lett.* 41, 5978–5986.  
949 <https://doi.org/10.1002/2014GL060527>
- 950 Mantsis, D., Clement, A., 2009. Simulated variability in the mean atmospheric meridional  
951 circulation over the 20th century. *Geophys. Res. Lett.* 36.  
952 <https://doi.org/10.1029/2008GL036741>
- 953 Mantua, N.J., Hare, S.R., Zhang, Y., Wallace, J.M., Francis, R.C., 1997. A Pacific Interdecadal  
954 Climate Oscillation with Impacts on Salmon Production\*. *Bull. Am. Meteorol. Soc.* 78,  
955 1069–1080. [https://doi.org/10.1175/1520-](https://doi.org/10.1175/1520-0477(1997)078<1069:APICOW>2.0.CO;2)  
956 [0477\(1997\)078<1069:APICOW>2.0.CO;2](https://doi.org/10.1175/1520-0477(1997)078<1069:APICOW>2.0.CO;2)
- 957 Marotzke, J., Forster, P.M., 2015. Forcing, feedback and internal variability in global  
958 temperature trends. *Nature* 517, 565–570. <https://doi.org/10.1038/nature14117>
- 959 Marshall, J., Armour, K.C., Scott, J.R., Kostov, Y., Hausmann, U., Ferreira, D., Shepherd, T.G.,  
960 Bitz, C.M., 2014. The ocean’s role in polar climate change: asymmetric Arctic and  
961 Antarctic responses to greenhouse gas and ozone forcing. *Philos. Trans. R. Soc. Math.*  
962 *Phys. Eng. Sci.* 372, 20130040. <https://doi.org/10.1098/rsta.2013.0040>
- 963 Medhaug, I., Stolpe, M.B., Fischer, E.M., Knutti, R., 2017. Reconciling controversies about the  
964 ‘global warming hiatus.’ *Nature* 545, 41–47. <https://doi.org/10.1038/nature22315>
- 965 Meehl, G.A., Arblaster, J.M., Fasullo, J.T., Hu, A., Trenberth, K.E., 2011. Model-based evidence  
966 of deep-ocean heat uptake during surface-temperature hiatus periods. *Nat. Clim.*  
967 *Change* 1, 360–364. <https://doi.org/10.1038/NCLIMATE1229>
- 968 Menary, M.B., Hodson, D.L.R., Robson, J.I., Sutton, R.T., Wood, R.A., Hunt, J.A., 2015.  
969 Exploring the impact of CMIP5 model biases on the simulation of North Atlantic  
970 decadal variability. *Geophys. Res. Lett.* 42, 5926–5934.  
971 <https://doi.org/10.1002/2015GL064360>
- 972 Moreno-Chamarro, E., Zanchettin, D., Lohmann, K., Jungclaus, J.H., 2015. Internally  
973 generated decadal cold events in the northern North Atlantic and their possible

974 implications for the demise of the Norse settlements in Greenland. *Geophys. Res.*  
975 *Lett.* 2014GL062741. <https://doi.org/10.1002/2014GL062741>

976 Morice, C.P., Kennedy, J.J., Rayner, N.A., Jones, P.D., 2012. Quantifying uncertainties in global  
977 and regional temperature change using an ensemble of observational estimates: The  
978 HadCRUT4 data set. *J. Geophys. Res. Atmospheres* 1984–2012 117.

979 Muir, L.C., Fedorov, A.V., 2015. How the AMOC affects ocean temperatures on decadal to  
980 centennial timescales: the North Atlantic versus an interhemispheric seesaw. *Clim.*  
981 *Dyn.* 45, 151–160. <https://doi.org/10.1007/s00382-014-2443-7>

982 Neukom, R., Gergis, J., Karoly, D.J., Wanner, H., Curran, M., Elbert, J., González-Rouco, F.,  
983 Linsley, B.K., Moy, A.D., Mundo, I., Raible, C.C., Steig, E.J., van Ommen, T., Vance, T.,  
984 Villalba, R., Zinke, J., Frank, D., 2014. Inter-hemispheric temperature variability over  
985 the past millennium. *Nat. Clim. Change* 4, 362–367.  
986 <https://doi.org/10.1038/nclimate2174>

987 Neukom, R., Schurer, A.P., Steiger, N.J., Hegerl, G.C., 2018. Possible causes of data model  
988 discrepancy in the temperature history of the last Millennium. *Sci. Rep.* 8, 7572.  
989 <https://doi.org/10.1038/s41598-018-25862-2>

990 Overland, J., Rodionov, S.N., Minobe, S., Bond, N., 2008. North Pacific regime shifts:  
991 Definitions, issues and recent transitions. *Prog. Oceanogr.* 77, 92–102.  
992 <https://doi.org/10.1016/j.pocean.2008.03.016>

993 Park, T., Park, W., Latif, M., 2016. Correcting North Atlantic sea surface salinity biases in the  
994 Kiel Climate Model: influences on ocean circulation and Atlantic Multidecadal  
995 Variability. *Clim. Dyn.* 47, 2543–2560. <https://doi.org/10.1007/s00382-016-2982-1>

996 Parker, D., Folland, C., Scaife, A., Knight, J., Colman, A., Baines, P., Dong, B., 2007. Decadal to  
997 multidecadal variability and the climate change background. *J. Geophys. Res.*  
998 *Atmospheres* 112. <https://doi.org/10.1029/2007JD008411>

999 Polson, D., Bollasina, M., Hegerl, G.C., Wilcox, L.J., 2014. Decreased monsoon precipitation in  
1000 the Northern Hemisphere due to anthropogenic aerosols. *Geophys. Res. Lett.* 41,  
1001 6023–6029. <https://doi.org/10.1002/2014GL060811>

1002 Polson, D., Hegerl, G.C., Solomon, S., 2016. Precipitation sensitivity to warming estimated  
1003 from long island records. *Environ. Res. Lett.* 11, 074024.  
1004 <https://doi.org/10.1088/1748-9326/11/7/074024>

1005 Power, S., Casey, T., Folland, C., Colman, A., Mehta, V., 1999. Inter-decadal modulation of the  
1006 impact of ENSO on Australia. *Clim. Dyn.* 15, 319–324.  
1007 <https://doi.org/10.1007/s003820050284>

1008 Rahmstorf, S., Box, J.E., Feulner, G., Mann, M.E., Robinson, A., Rutherford, S., Schaffernicht,  
1009 E.J., 2015. Exceptional twentieth-century slowdown in Atlantic Ocean overturning  
1010 circulation. *Nat. Clim. Change* 5, 475–480. <https://doi.org/10.1038/nclimate2554>

1011 Rajesh, R., Tiwari, R.K., 2018. Search for Trends and Periodicities in Inter-hemispheric Sea  
1012 Surface Temperature Difference. *Pure Appl. Geophys.* 175, 2381–2394.  
1013 <https://doi.org/10.1007/s00024-018-1791-3>

1014 Reverdin, G., Friedman, A.R., Chafik, L., Holliday, N.P., Szekely, T., Valdimarsson, H.,  
1015 Yashayaev, I., 2019. North Atlantic extratropical and subpolar gyre variability during  
1016 the last 120 years: a gridded dataset of surface temperature, salinity, and density.  
1017 Part 1: dataset validation and RMS variability. *Ocean Dyn.* 69, 385–403.  
1018 <https://doi.org/10.1007/s10236-018-1240-y>



1019 Rotstayn, L., Lohmann, U., 2002. Tropical rainfall trends and the indirect aerosol effect. *J.*  
1020 *Clim.* 15, 2103–2116.

1021 Rotstayn, L.D., Collier, M.A., Chrastansky, A., Jeffrey, S.J., Luo, J.-J., 2013. Projected effects of  
1022 declining aerosols in RCP4.5: unmasking global warming? *Atmos Chem Phys* 13,  
1023 10883–10905. <https://doi.org/10.5194/acp-13-10883-2013>

1024 Rotstayn, L.D., Collier, M.A., Luo, J.-J., 2015. Effects of declining aerosols on projections of  
1025 zonally averaged tropical precipitation. *Environ. Res. Lett.* 10, 044018.  
1026 <https://doi.org/10.1088/1748-9326/10/4/044018>

1027 Saba, V.S., Griffies, S.M., Anderson, W.G., Winton, M., Alexander, M.A., Delworth, T.L., Hare,  
1028 J.A., Harrison, M.J., Rosati, A., Vecchi, G.A., Zhang, R., 2016. Enhanced warming of the  
1029 Northwest Atlantic Ocean under climate change. *J. Geophys. Res. Oceans* 121, 118–  
1030 132. <https://doi.org/10.1002/2015JC011346>

1031 Santer, B.D., Wigley, T.M.L., Boyle, J.S., Gaffen, D.J., Hnilo, J.J., Nychka, D., Parker, D.E., Taylor,  
1032 K.E., 2000. Statistical significance of trends and trend differences in layer-average  
1033 atmospheric temperature time series. *J. Geophys. Res. Atmospheres* 105, 7337–  
1034 7356. <https://doi.org/10.1029/1999JD901105>

1035 Schneider, T., Bischoff, T., Haug, G.H., 2014. Migrations and dynamics of the intertropical  
1036 convergence zone. *Nature* 513, 45–53. <https://doi.org/10.1038/nature13636>

1037 Schneider, U., Becker, A., Finger, P., Meyer-Christoffer, A., Ziese, M., 2018. GPCP Full Data  
1038 Monthly Version 2018.0 at 2.5°: Monthly Land-Surface Precipitation from Rain-  
1039 Gauges built on GTS-based and Historic Data.  
1040 [https://doi.org/10.5676/dwd\\_gpcc/fd\\_m\\_v2018\\_250](https://doi.org/10.5676/dwd_gpcc/fd_m_v2018_250)

1041 Schurer, A., Hegerl, G., Ribes, A., Polson, D., Morice, C., Tett, S., 2018. Estimating the  
1042 Transient Climate Response from Observed Warming. *J. Clim.* 31, 8645–8663.  
1043 <https://doi.org/10.1175/JCLI-D-17-0717.1>

1044 Schurer, A.P., Hegerl, G.C., Mann, M.E., Tett, S.F.B., Phipps, S.J., 2013. Separating Forced from  
1045 Chaotic Climate Variability over the Past Millennium. *J. Clim.* 26, 6954–6973.  
1046 <https://doi.org/10.1175/JCLI-D-12-00826.1>

1047 Schurer, A.P., Hegerl, G.C., Obrochta, S.P., 2015. Determining the likelihood of pauses and  
1048 surges in global warming. *Geophys. Res. Lett.* 42, 2015GL064458.  
1049 <https://doi.org/10.1002/2015GL064458>

1050 Schurer, A.P., Tett, S.F.B., Hegerl, G.C., 2014. Small influence of solar variability on climate  
1051 over the past millennium. *Nat. Geosci.* 7, 104–108.  
1052 <https://doi.org/10.1038/ngeo2040>

1053 Sen Gupta, A., Jourdain, N.C., Brown, J.N., Monselesan, D., 2013. Climate Drift in the CMIP5  
1054 Models. *J. Clim.* 26, 8597–8615. <https://doi.org/10.1175/JCLI-D-12-00521.1>

1055 Serreze, M.C., Barry, R.G., 2011. Processes and impacts of Arctic amplification: A research  
1056 synthesis. *Glob. Planet. Change* 77, 85–96.  
1057 <https://doi.org/10.1016/j.gloplacha.2011.03.004>

1058 Servain, J., Wainer, I., McCreary, J.P., Dessier, A., 1999. Relationship between the equatorial  
1059 and meridional modes of climatic variability in the tropical Atlantic. *Geophys. Res.*  
1060 *Lett.* 26, 485–488. <https://doi.org/10.1029/1999GL900014>

1061 Sgubin, G., Swingedouw, D., Drijfhout, S., Mary, Y., Bennabi, A., 2017. Abrupt cooling over  
1062 the North Atlantic in modern climate models. *Nat. Commun.* 8.  
1063 <https://doi.org/10.1038/ncomms14375>

1064 Stevens, B., 2015. Rethinking the Lower Bound on Aerosol Radiative Forcing. *J. Clim.* 28,  
1065 4794–4819. <https://doi.org/10.1175/JCLI-D-14-00656.1>

1066 Stouffer, R., Manabe, S., Bryan, K., 1989. Interhemispheric Asymmetry In Climate Response  
1067 To A Gradual Increase Of Atmospheric CO<sub>2</sub>. *Nature* 342, 660–662.

1068 Stouffer, R.J., Seidov, D., Haupt, B.J., 2007. Climate Response to External Sources of  
1069 Freshwater: North Atlantic versus the Southern Ocean. *J. Clim.* 20, 436–448.  
1070 <https://doi.org/10.1175/JCLI4015.1>

1071 Sun, C., Li, J., Jin, F.-F., Ding, R., 2013. Sea surface temperature inter-hemispheric dipole and  
1072 its relation to tropical precipitation. *Environ. Res. Lett.* 8, 044006.  
1073 <https://doi.org/10.1088/1748-9326/8/4/044006>

1074 Sun, C., Li, J., Li, X., Xue, J., Ding, R., Xie, F., Li, Y., 2018. Oceanic forcing of the  
1075 interhemispheric SST dipole associated with the Atlantic Multidecadal Oscillation.  
1076 *Environ. Res. Lett.* 13, 074026. <https://doi.org/10.1088/1748-9326/aacf66>

1077 Swingedouw, D., Mignot, J., Labetoulle, S., Guilyardi, E., Madec, G., 2013. Initialisation and  
1078 predictability of the AMOC over the last 50 years in a climate model. *Clim. Dyn.* 40,  
1079 2381–2399. <https://doi.org/10.1007/s00382-012-1516-8>

1080 Swingedouw, D., Mignot, J., Ortega, P., Khodri, M., Menegoz, M., Cassou, C., Hanquiez, V.,  
1081 2017. Impact of explosive volcanic eruptions on the main climate variability modes.  
1082 *Glob. Planet. Change* 150, 24–45. <https://doi.org/10.1016/j.gloplacha.2017.01.006>

1083 Taylor, K.E., Stouffer, R.J., Meehl, G.A., 2012. An Overview of CMIP5 and the Experiment  
1084 Design. *Bull. Am. Meteorol. Soc.* 93, 485–498. <https://doi.org/10.1175/BAMS-D-11-00094.1>

1085

1086 Terray, L., 2012. Evidence for multiple drivers of North Atlantic multi-decadal climate  
1087 variability. *Geophys. Res. Lett.* 39. <https://doi.org/10.1029/2012GL053046>

1088 Tett, S.F.B., Jones, G.S., Stott, P.A., Hill, D.C., Mitchell, J.F.B., Allen, M.R., Ingram, W.J., Johns,  
1089 T.C., Johnson, C.E., Jones, A., Roberts, D.L., Sexton, D.M.H., Woodage, M.J., 2002.  
1090 Estimation of natural and anthropogenic contributions to twentieth century  
1091 temperature change. *J. Geophys. Res. Atmospheres* 107, ACL 10-1-ACL 10-24.  
1092 <https://doi.org/10.1029/2000JD000028>

1093 Thibodeau, B., Not, C., Zhu, J., Schmittner, A., Noone, D., Tabor, C., Zhang, J., Liu, Z., 2018. Last  
1094 Century Warming Over the Canadian Atlantic Shelves Linked to Weak Atlantic  
1095 Meridional Overturning Circulation. *Geophys. Res. Lett.* 45, 12,376-12,385.  
1096 <https://doi.org/10.1029/2018GL080083>

1097 Thompson, D.W.J., Wallace, J.M., Jones, P.D., Kennedy, J.J., 2009. Identifying Signatures of  
1098 Natural Climate Variability in Time Series of Global-Mean Surface Temperature:  
1099 Methodology and Insights. *J. Clim.* 22, 6120–6141.  
1100 <https://doi.org/10.1175/2009JCLI3089.1>

1101 Thompson, D.W.J., Wallace, J.M., Kennedy, J.J., Jones, P.D., 2010. An abrupt drop in Northern  
1102 Hemisphere sea surface temperature around 1970. *Nature* 467, 444–447.  
1103 <https://doi.org/10.1038/nature09394>

1104 Thornalley, D.J.R., Oppo, D.W., Ortega, P., Robson, J.I., Brierley, C.M., Davis, R., Hall, I.R.,  
1105 Moffa-Sanchez, P., Rose, N.L., Spooner, P.T., Yashayaev, I., Keigwin, L.D., 2018.  
1106 Anomalously weak Labrador Sea convection and Atlantic overturning during the  
1107 past 150 years. *Nature* 556, 227. <https://doi.org/10.1038/s41586-018-0007-4>

1108 Trottini, M., Isabel, M., Aguiar, V., Palazón, S.B., 2015. On the Use of Running Trends as  
1109 Summary Statistics for Univariate Time Series and Time Series Association. *J. Clim.*  
1110 28, 7489–7502. <https://doi.org/10.1175/JCLI-D-15-0009.1>  
1111 Undorf, S., Polson, D., Bollasina, M.A., Ming, Y., Schurer, A., Hegerl, G.C., 2018. Detectable  
1112 Impact of Local and Remote Anthropogenic Aerosols on the 20th Century Changes of  
1113 West African and South Asian Monsoon Precipitation. *J. Geophys. Res.-*  
1114 *ATMOSPHERES* 123, 4871–4889. <https://doi.org/10.1029/2017JD027711>  
1115 Vellinga, M., Wu, P., 2004. Low-Latitude Freshwater Influence on Centennial Variability of  
1116 the Atlantic Thermohaline Circulation. *J. Clim.* 17, 4498–4511.  
1117 <https://doi.org/10.1175/3219.1>  
1118 Vuuren, D.P. van, Edmonds, J., Kainuma, M., Riahi, K., Thomson, A., Hibbard, K., Hurtt, G.C.,  
1119 Kram, T., Krey, V., Lamarque, J.-F., Masui, T., Meinshausen, M., Nakicenovic, N., Smith,  
1120 S.J., Rose, S.K., 2011. The representative concentration pathways: an overview. *Clim.*  
1121 *Change* 109, 5–31. <https://doi.org/10.1007/s10584-011-0148-z>  
1122 Wang, B., Liu, J., Kim, H.-J., Webster, P.J., Yim, S.-Y., 2012. Recent change of the global  
1123 monsoon precipitation (1979–2008). *Clim. Dyn.* 39, 1123–1135.  
1124 <https://doi.org/10.1007/s00382-011-1266-z>  
1125 Wang, R., Balkanski, Y., Boucher, O., Ciais, P., Schuster, G.L., Chevallier, F., Samset, B.H., Liu,  
1126 J., Piao, S., Valari, M., Tao, S., 2016. Estimation of global black carbon direct radiative  
1127 forcing and its uncertainty constrained by observations. *J. Geophys. Res.*  
1128 *Atmospheres* 121, 5948–5971. <https://doi.org/10.1002/2015JD024326>  
1129 Wang, Z., Zhang, X., Guan, Z., Sun, B., Yang, X., Liu, C., 2015. An atmospheric origin of the  
1130 multi-decadal bipolar seesaw. *Sci. Rep.* 5, 8909. <https://doi.org/10.1038/srep08909>  
1131 Wilcox, L.J., Highwood, E.J., Dunstone, N.J., 2013. The influence of anthropogenic aerosol on  
1132 multi-decadal variations of historical global climate. *Environ. Res. Lett.* 8, 024033.  
1133 <https://doi.org/10.1088/1748-9326/8/2/024033>  
1134 Wilks, D.S., 2016. “The Stippling Shows Statistically Significant Grid Points”: How Research  
1135 Results are Routinely Overstated and Overinterpreted, and What to Do about It. *Bull.*  
1136 *Am. Meteorol. Soc.* 97, 2263–2273. <https://doi.org/10.1175/BAMS-D-15-00267.1>  
1137 Xie, S.-P., 2016. Oceanography: Leading the hiatus research surge. *Nat. Clim. Change* 6, 345–  
1138 346. <https://doi.org/10.1038/nclimate2973>  
1139 Xie, S.P., Carton, J.A., 2004. Tropical Atlantic variability: Patterns, mechanisms, and impacts,  
1140 in: *Earth’s Climate: The Ocean-Atmosphere Interaction*, *Geophys. Monogr.*  
1141 *Geophysical Monograph Series*. pp. 121–142.  
1142 Xu, Y., Ramanathan, V., 2012. Latitudinally asymmetric response of global surface  
1143 temperature: Implications for regional climate change. *Geophys. Res. Lett.* 39.  
1144 <https://doi.org/10.1029/2012GL052116>  
1145 Xue, J., Sun, C., Li, J., Mao, J., Nakamura, H., Miyasaka, T., Xu, Y., 2018. Divergent Responses of  
1146 Extratropical Atmospheric Circulation to Interhemispheric Dipolar SST Forcing over  
1147 the Two Hemispheres in Boreal Winter. *J. Clim.* 31, 7599–7619.  
1148 <https://doi.org/10.1175/JCLI-D-17-0817.1>  
1149 Yan, X.-H., Boyer, T., Trenberth, K., Karl, T.R., Xie, S.-P., Nieves, V., Tung, K.-K., Roemmich, D.,  
1150 2016. The global warming hiatus: Slowdown or redistribution? *Earths Future* 4,  
1151 472–482. <https://doi.org/10.1002/2016EF000417>

1152 Zhang, R., Delworth, T.L., 2007. Impact of the Atlantic Multidecadal Oscillation on North  
1153 Pacific climate variability. *Geophys. Res. Lett.* 34, L23708.  
1154 <https://doi.org/10.1029/2007GL031601>  
1155 Zhang, Y., Wallace, J.M., Battisti, D.S., 1997. ENSO-like Interdecadal Variability: 1900–93. *J.*  
1156 *Clim.* 10, 1004–1020. [https://doi.org/10.1175/1520-](https://doi.org/10.1175/1520-0442(1997)010<1004:ELIV>2.0.CO;2)  
1157 [0442\(1997\)010<1004:ELIV>2.0.CO;2](https://doi.org/10.1175/1520-0442(1997)010<1004:ELIV>2.0.CO;2)  
1158  
  
1159

1160 **Table 1: Models investigated.** CMIP5 groups and models are listed with the number of historical and historicalNat realizations; the  
 1161 length of the piControl simulations; and the number of 132-year segments from the control simulations used in the analysis.

			<b>Historical, HistoricalNat</b>	<b>piControl</b>	
	<b>Group</b>	<b>Model</b>	<b>Realizations</b>	<b>length (yrs.)</b>	<b>segments</b>
1164	BCC	bcc-csm1-1	1	500	3
1165	CCCma	CanESM2	5	996	7
1166	CNRM-CERFACS	CNRM-CM5	6	850	6
1167	CSIRO-QCCCE	CSIRO-Mk3-6-0	5	500	3
1168	IPSL	IPSL-CM5A-LR	3	1000	7
1169	IPSL	IPSL-CM5A-MR	1	300	2
1170	MOHC	HadGEM2-ES	4	576	4
1171	NASA-GISS	GISS-E2-H	5	540	4
1172	NASA-GISS	GISS-E2-R	5	500	3
1173	NCC	NorESM1-M	1	501	3
1174	NCAR	CCSM4		1051	7
1175	NOAA-GFDL	GFDL-CM3		500	3

1176 **Table 2: Detection and attribution scaling factors.** Best-estimate scaling factors and 5-95%  
 1177 confidence intervals for natural (left) and anthropogenic (right) forcing for the (a)  
 1178 interhemispheric SST contrast and (b) NH and SH individually. Bold coefficients are detected at  
 1179 a 95% significance level, and asterisks indicate where the confidence intervals are outside the  
 1180 multimodel mean.

1181

1182 **(a) NH-SH**

	$\beta_{Nat}$	$\beta_{Ant}$
1183 HadSST3:	1.14 (-0.3 to 2.2)	<b>1.32</b> (0.7 to 2.6)
1184 ERSSTv5:	0.30 (-1.2 to 1.4)	<b>1.90</b> (1.2 to 3.3) *

1186

1187 **(b) NH and SH**

	$\beta_{Nat}$	$\beta_{Ant}$
1188 <b><u>NH</u></b>		
1189 HadSST3:	<b>0.57</b> (0.1 to 1.0)	<b>1.13</b> (0.8 to 1.5)
1190 ERSSTv5:	0.28 (-0.2 to 0.7)	<b>1.20</b> (0.9 to 1.5)
1191 <b><u>SH</u></b>		
1192 HadSST3:	<b>0.40</b> (+0.0 to 0.7) *	<b>1.19</b> (1.1 to 1.4) *
1193 ERSSTv5:	-0.22 (-0.6 to 0.1)	<b>1.32</b> (1.2 to 1.5) *

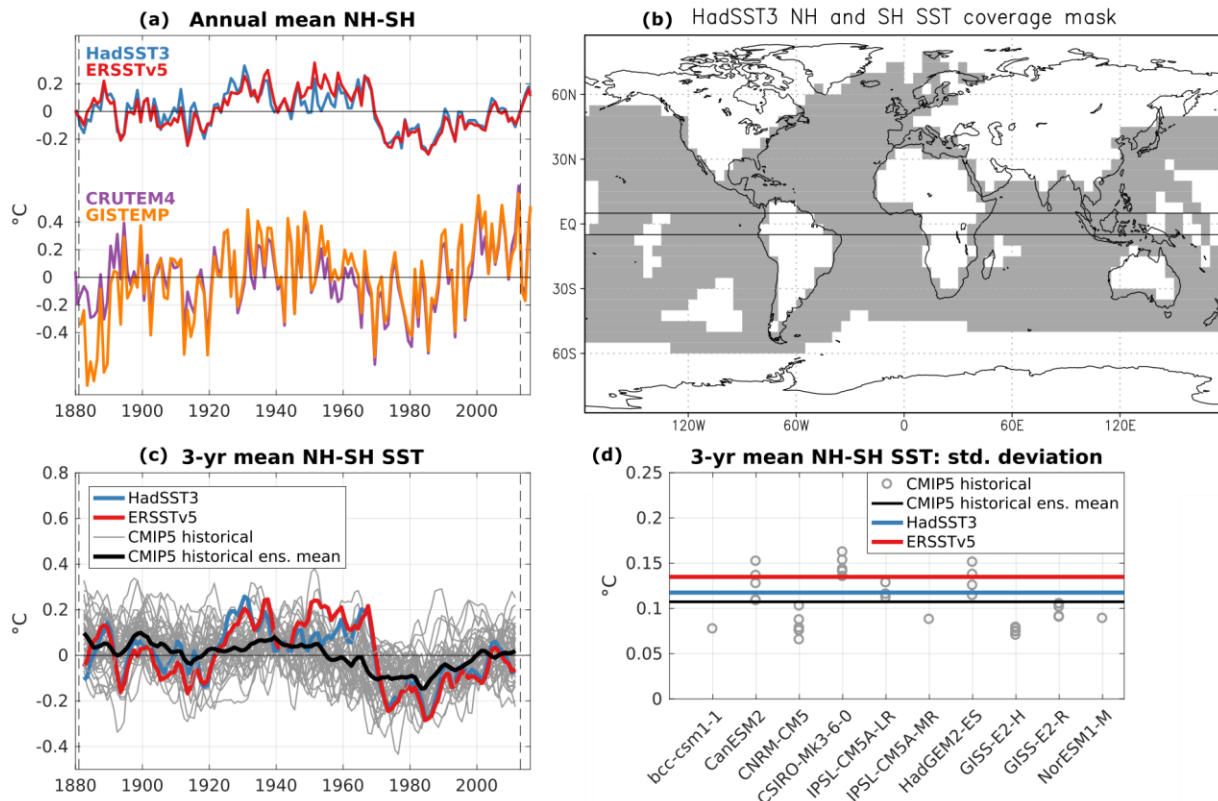
1194

1195 **Table 3. 1970 and 1920s trend magnitudes.** 9-year observational and best-estimate residual  
 1196 SST trend magnitudes over 1966–1974 and 1918–1926 for the interhemispheric SST contrast,  
 1197 the NH, and the SH, in °C per decade.

1198

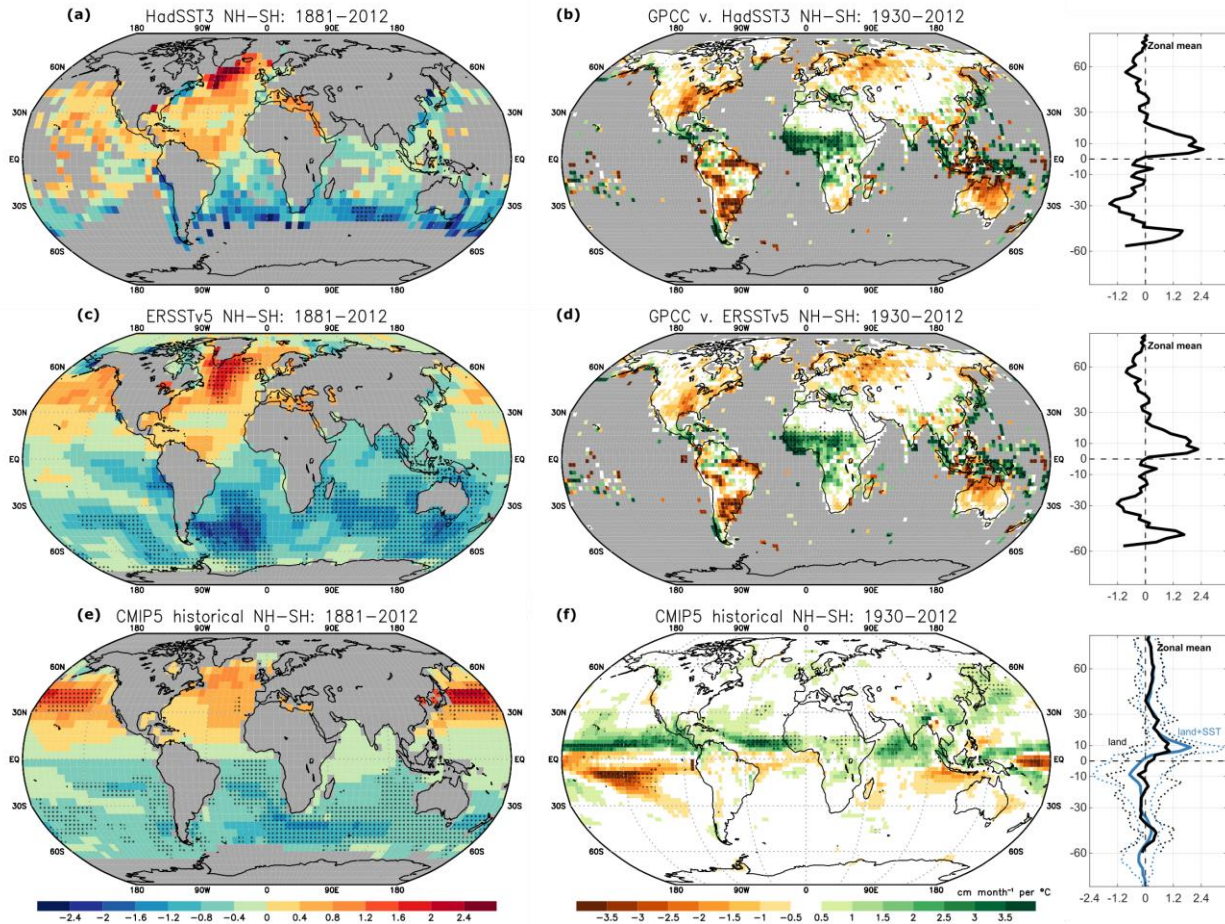
	<b>Observations</b>		<b>Best-estimate residual</b>	
<b>1966–1974</b>	<b>HadSST3</b>	<b>ERSSTv5</b>	<b>HadSST3</b>	<b>ERSSTv5</b>
<b>NH-SH</b>	–0.61	–0.64	–0.53	–0.49
<b>NH</b>	–0.34	–0.25	–0.40	–0.27
<b>SH</b>	0.27	0.40	0.15	0.34
<b>1918–1926</b>	<b>HadSST3</b>	<b>ERSSTv5</b>	<b>HadSST3</b>	<b>ERSSTv5</b>
<b>NH-SH</b>	0.42	0.30	0.40	0.21
<b>NH</b>	0.29	0.17	0.22	0.08
<b>SH</b>	–0.13	–0.12	–0.17	–0.18

1208



1209  
 1210 **Figure 1. Interhemispheric temperature and SST contrast time series.** (a) Top: annual mean  
 1211 (December–November) interhemispheric SST contrast anomaly of HadSST3 (blue) and  
 1212 ERSSTv5 (red). Bottom: land surface interhemispheric contrast anomaly of CRUTEM4 (purple)  
 1213 and GISTEMP (orange). Anomalies are from 1881–2012 (vertical dashed lines). (b) Gridpoints  
 1214 included in computing the northern and southern hemisphere SST means, based on HadSST3  
 1215 data coverage and poleward of 5° latitude (solid lines). (c) 3-year running mean interhemispheric  
 1216 SST contrast anomaly of CMIP5 historical realizations and observations. Thin lines show  
 1217 individual realizations; the solid black line shows the multimodel ensemble mean. (d) 1881–2012  
 1218 standard deviations of the 3-year mean interhemispheric SST contrast of observations and  
 1219 historical realizations from (c). Grey circles show individual realizations; the solid black line  
 1220 shows the multimodel ensemble mean.





1221

1222 **Figure 2. Interhemispheric SST contrast spatial patterns: SST and rainfall.** (a, c, e) Slope of

1223 3-year mean SST v. interhemispheric SST contrast from 1881-2012 (from **Figure 1c**) for (a)

1224 HadSST3, (c) ERSSTv5, and (e) CMIP5 historical ensemble mean, in  $^{\circ}\text{C}$  per  $^{\circ}\text{C}$  (unitless). (b, d,

1225 f) Slope of 3-year mean precipitation v. interhemispheric SST contrast for (b) GPCC rainfall and

1226 HadSST3 from 1930–2012, (d) GPCC rainfall and ERSSTv5 from 1930–2012, and (f) CMIP5

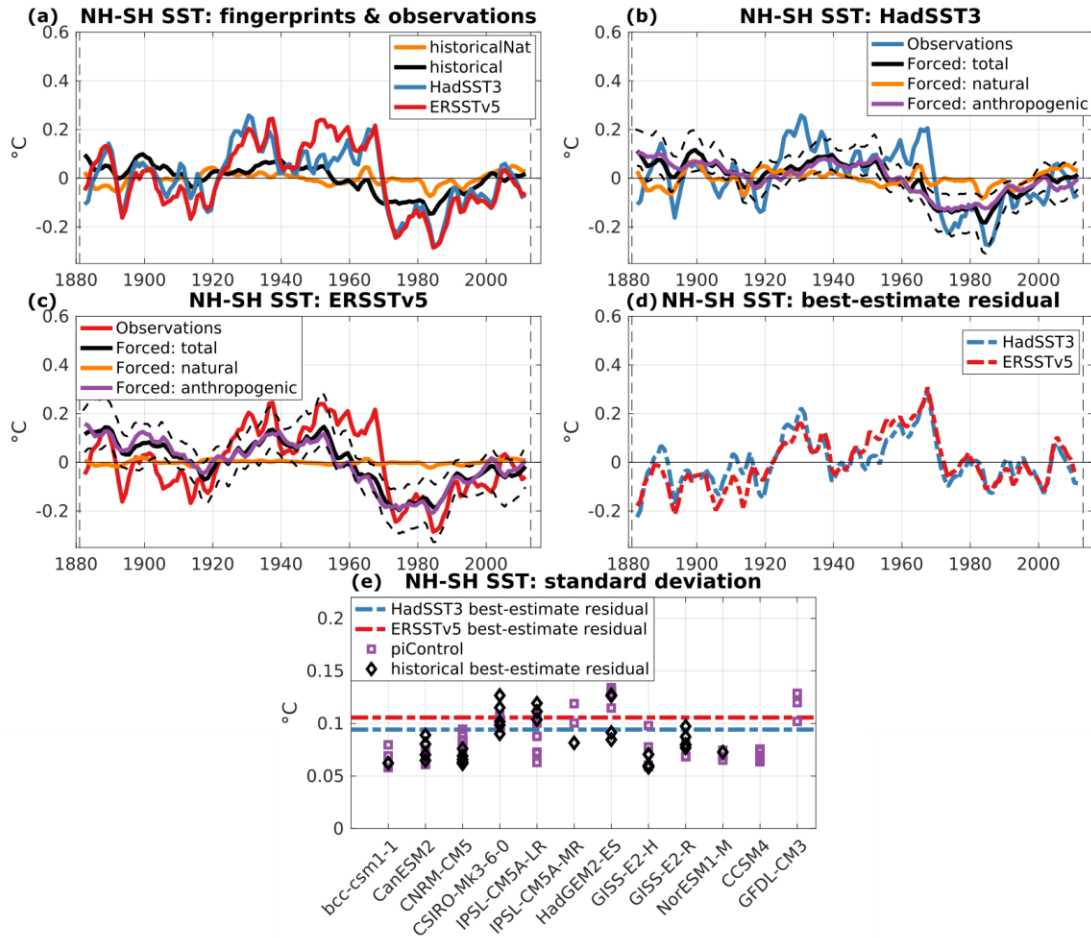
1227 historical mean from 1930–2012, in  $\text{cm month}^{-1}$  per  $^{\circ}\text{C}$ . Right panels show the zonal mean

1228 slopes. Stippling in (a)–(d) indicates where the slope is significant at  $p < 0.05$  and satisfying  $\alpha_{\text{FDR}}$

1229  $= 0.05$  (see text). Stippling in (e) and (f) indicates sign agreement of at least 30 out of 36

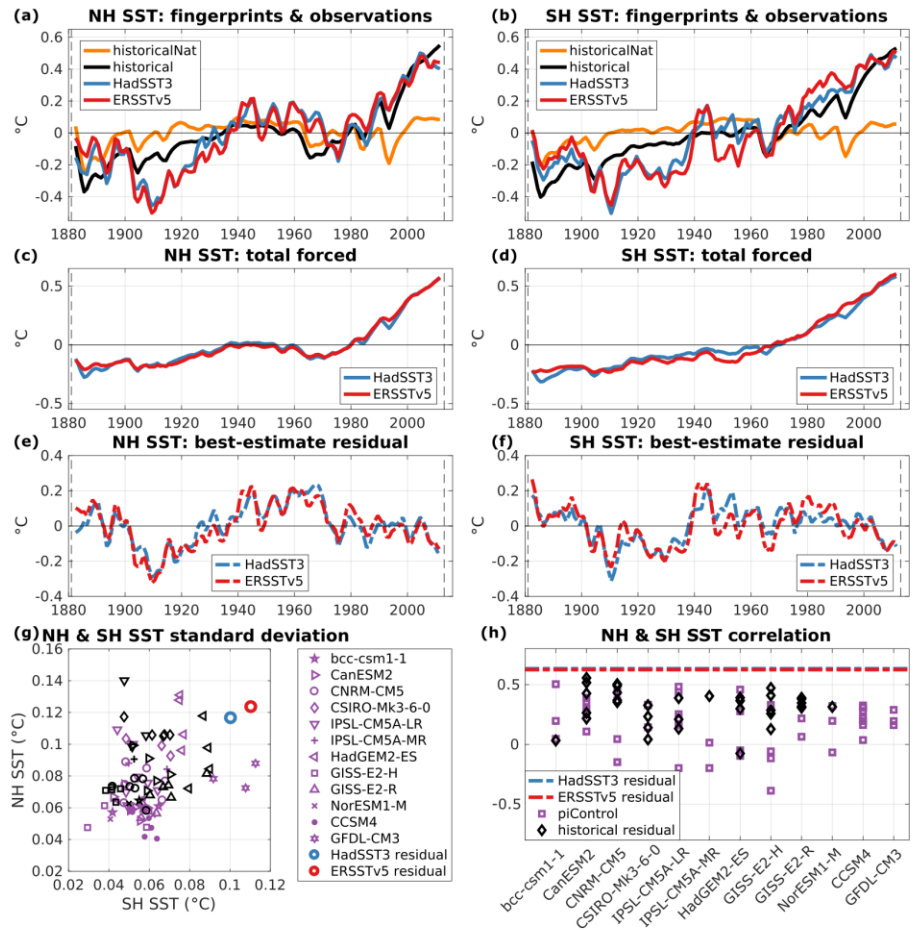
1230 realizations. Colors in the right panel of (f) indicate land + SST (blue) and land only (black)

1231 slopes; dotted lines enclose the middle 30 out of 36 realizations.



1232

1233 **Figure 3. Interhemispheric SST contrast detection and attribution.** (a) 3-year mean  
 1234 interhemispheric SST contrast anomaly: historicalNat and historical fingerprints, and  
 1235 observations. (b-c) Forced component of the interhemispheric SST contrast for (b) HadSST3 and  
 1236 (c) ERSSTv5. Thick black line is the best-estimate forced component; thin dashed lines indicate  
 1237 the 5-95% confidence intervals (see text). The components from anthropogenic and natural  
 1238 forcing are also shown. (d) Best-estimate residual interhemispheric SST contrast time series for  
 1239 HadSST3 and ERSSTv5. (e) Standard deviations of the best-estimate observational residuals,  
 1240 control simulations, and best-estimate historical realization residuals.



1241

1242 **Figure 4. Separate northern and southern hemisphere SST detection and attribution. (a-b)**

1243 3-year mean (a) NH and (b) SH SST anomalies: historicalNat and historical fingerprints, and

1244 observations. (c-d) Total forced component of the (c) NH and (d) SH SST. (e-f) Best-estimate

1245 residual SST time series for the (e) NH and (f) SH. (g) Standard deviations of NH and SH SST

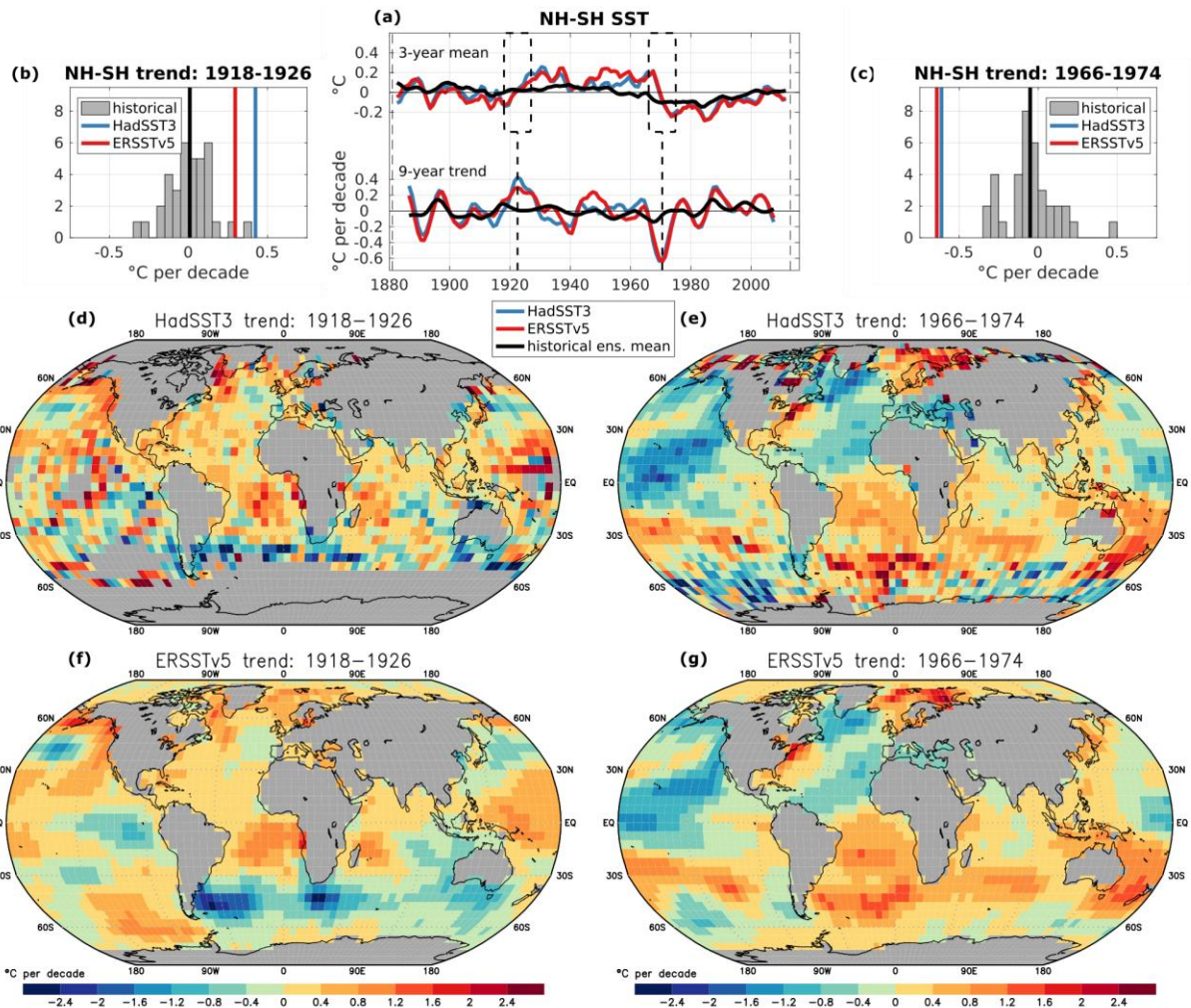
1246 from best-estimate observational residuals, control simulations, and best-estimate historical

1247 realization residuals. Purple markers show the control simulations, and black markers show the

1248 best-estimate historical simulation residuals. (h) Correlations of best-estimate residual NH and

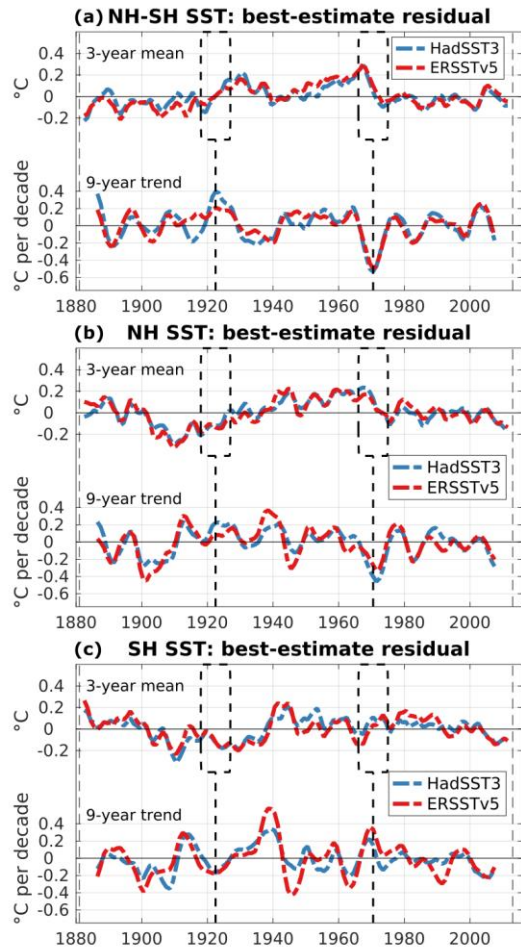
1249 SH SST with those of control simulations and best-estimate historical simulation residuals.

1250



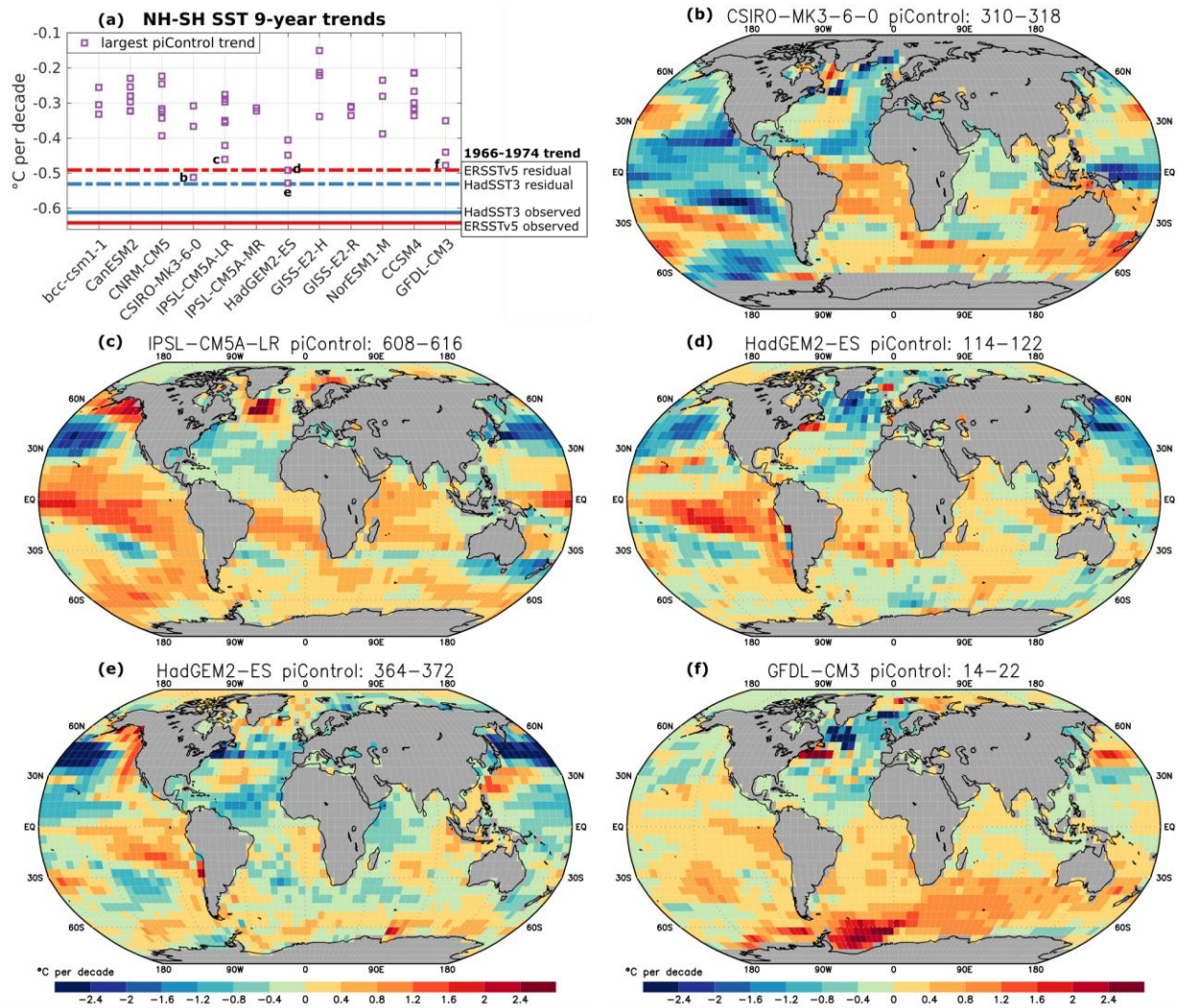
1251  
 1252 **Figure 5. Early-1920s and 1970 interhemispheric SST shifts.** (a) Top: 3-year mean  
 1253 interhemispheric SST contrast anomaly for HadSST3 (blue), ERSSTv5 (red), and CMIP5  
 1254 historical multimodel ensemble mean (black), in  $^{\circ}\text{C}$ . Bottom: 9-year running mean trends, in  $^{\circ}\text{C}$   
 1255 per decade. The dashed vertical lines indicate the trends centered in 1922 and 1970. (b–c)  
 1256 Distribution of 9-year interhemispheric SST trends of each CMIP5 historical realization  
 1257 compared with observations for (b) 1918–1926 and (c) 1966–1974. The multimodel ensemble  
 1258 mean is shown as a solid black line. (d, f) 9-year SST trend for the period centered in 1922 for  
 1259 (d) HadSST3 and (f) ERSSTv5, in  $^{\circ}\text{C}$  per decade. (e, g) Same as (d, f), but for the trend centered  
 1260 in 1970.

1261



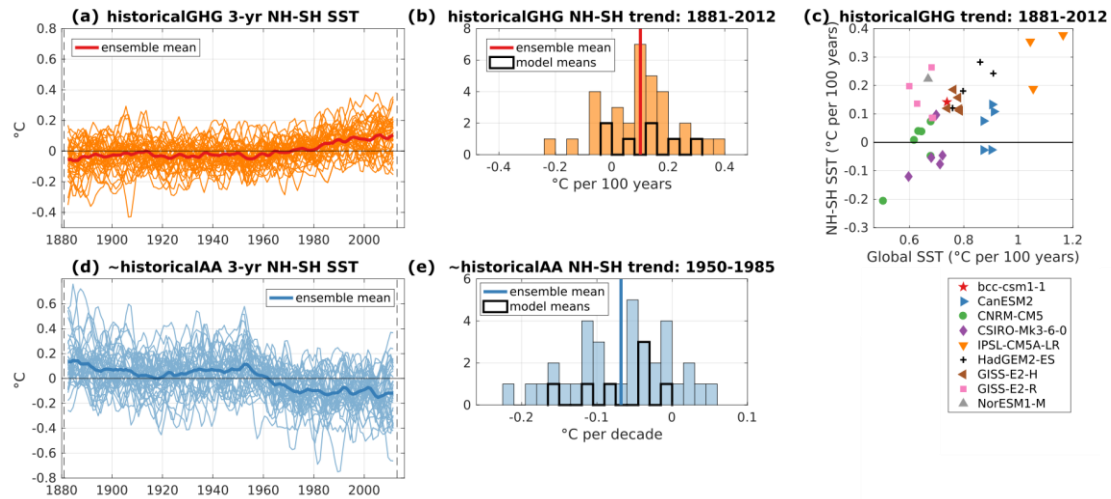
1262

1263 **Figure 6. Best-estimate residual SST running trends.** (a) 3-year mean best-estimate residual  
1264 interhemispheric SST contrast for HadSST3 and ERSSTv5 in °C (top), with 9-year running  
1265 mean trends in °C per decade (bottom). The dashed vertical lines indicate the trends centered in  
1266 1922 and 1970. (b-c) Same as (a), but for the (b) NH (c) SH SST.



1267

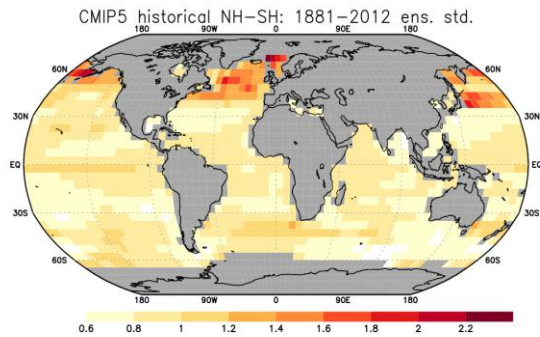
1268 **Figure 7. Control simulation interhemispheric SST shifts.** (a) Comparison of the observed  
 1269 and best-estimate residual interhemispheric SST trends from 1966–1974 with the largest-  
 1270 magnitude negative (SH–NH) 9-yr interhemispheric SST trend in each control segment, in °C  
 1271 per decade. (b–f) Spatial patterns of the largest-magnitude control segment trends, indicated by  
 1272 small letters in (a), in °C per decade: (b) CSIRO-Mk3-6-0 years 310–318, (c) IPSL-CM5A-LR  
 1273 years 608–616, (d) HadGEM2-ES years 114–122, (e) HadGEM2-ES years 364–372, and (f)  
 1274 GFDL-CM3 years 14–22.



1275

1276 **Figure 8. Specific-forcing interhemispheric SST time series.** (a) 3-year running  
 1277 historicalGHG interhemispheric SST contrast anomaly time series of 35 realizations. Thin lines  
 1278 show individual realizations; the thick red line shows the multi-model ensemble mean. (b)  
 1279 Distribution of 1881–2012 trends of each realization in (a). Individual model realizations are  
 1280 shaded orange; model means are outlined in black. The thick red line indicates the multimodel  
 1281 ensemble mean. (c) 1881-2012 interhemispheric SST contrast trends from (b) v. the respective  
 1282 1881-2012 global mean SST trends. (d) 3-year running mean historicalAA interhemispheric SST  
 1283 contrast anomaly approximation (historical–historicalGHG–historicalNat) of 35 realizations.  
 1284 Thin lines show individual realizations; thick line shows the multimodel ensemble mean. (e)  
 1285 Distribution of 1950–1985 trends of each realization in (d). Individual model realizations are  
 1286 shaded light blue; model means are outlined in black. The thick blue line indicates the  
 1287 multimodel ensemble mean.

1288



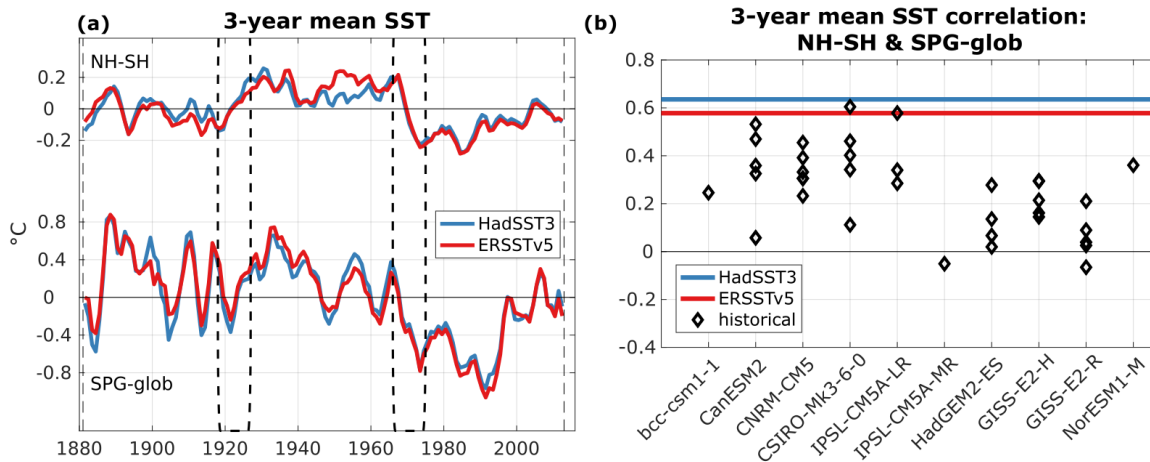
1289

1290 **Figure 9. Inter-model interhemispheric SST spatial pattern variability.** CMIP5 historical

1291 ensemble standard deviation of 3-year mean SST v. interhemispheric SST contrast from 1881-

1292 2012 (from **Figure 2e**), in  $^{\circ}\text{C}$  per  $^{\circ}\text{C}$  (unitless).

1293



1294

1295 **Figure 10. AMOC proxy SST index.** (a) Observed 3-year running mean interhemispheric SST

1296 contrast anomaly (top) and AMOC proxy SST index (subpolar North Atlantic SST minus global

1297 mean SST) anomaly (bottom; note different scaling). (b) Correlations of the interhemispheric

1298 SST contrast and AMOC proxy SST index in observations and historical simulations.